

Following excited-state chemical shifts in molecular ultrafast x-ray photoelectron spectroscopy

D. Mayer¹⁺, F. Lever¹⁺, D. Picconi^{2,*}, J. Metje¹, S. Alisauskas³, F. Calegari^{4,5,6}, S. Düsterer³, C. Ehler⁷, R. Feifel⁸, M. Niebuhr¹, B. Manschwetus³, M. Kuhlmann³, T. Mazza⁹, M. S. Robinson^{1,4}, R. J. Squibb⁸, A. Trabattoni⁴, M. Wallner⁸, P. Saalfrank², T. J. A. Wolf¹⁰ and M. Gühr^{1,*}

1 Institut für Physik und Astronomie, Universität Potsdam, 14476 Potsdam Germany

2 Institut für Chemie, Universität Potsdam, 14476 Potsdam Germany

3 Deutsches Elektronen Synchrotron (DESY), 22607 Hamburg, Germany

4 Center for Free-Electron Laser Science (CFEL), DESY, 22607 Hamburg, Germany

5 The Hamburg Centre for Ultrafast Imaging, Universität Hamburg, 22761 Hamburg, Germany

6 Institut für Experimentalphysik, Universität Hamburg, 22761 Hamburg, Germany

7 Heidelberg Institute for Theoretical Studies, HITS gGmbH, 69118 Heidelberg, Germany

8 Department of Physics, University of Gothenburg, SE-41296 Gothenburg, Sweden

9 European XFEL, 22869 Schenefeld, Germany

10 Stanford PULSE Institute, SLAC National Accelerator Laboratory, 94025 Menlo Park, United States of America

+ Contributed equally

* correspondence should be addressed to david.picconi@uni-potsdam.de and mguehr@uni-potsdam.de

Abstract

The conversion of photon energy into other energetic forms in molecules is accompanied by charge moving on ultrafast timescales. We directly observe the charge motion at a specific site in an electronically excited molecule using time-resolved x-ray photoelectron spectroscopy (TR-XPS). We extend the concept of static chemical shift from conventional XPS by the excited-state chemical shift (ESCS), which is connected to the charge in the framework of a potential model. This allows us to invert TR-XPS spectra to the dynamic charge at a specific atom.

We demonstrate the power of TR-XPS by using sulphur 2p-core-electron-emission probing to study the UV-excited dynamics of 2-thiouracil. The new method allows us to discover that a major part of the population relaxes to the molecular ground state within 220-250 fs. In addition, a 250-fs oscillation, visible in the kinetic energy of the TR-XPS, reveals a coherent exchange of population among electronic states.

Introduction

Light-induced charge flow in molecules forms the basis to convert photon energy into other energetic forms. The excitation of valence electrons by light triggers a change in charge density that eventually couples to nuclear motion. The complex interplay of nuclear and electronic degrees of freedom in the electronically excited states continues to move charge on an ultrafast time-scale by nonadiabatic couplings ¹. This in turn gives rise to phenomena like photoisomerization ² and proton-coupled electron transfer ³ with rich applications in light-harvesting and photocatalysis ⁴. Finding a way to image the charge flow in electronically excited systems, including organic molecules, on its natural time-scale and with atomic precision would provide new ground for understanding molecular photophysics and excited-state reactivity.

X-ray photoelectron spectroscopy (XPS) is a proven tool to obtain information about local charge with atomic specificity in electronic ground states ⁵. The tight localization of core orbitals makes the method site selective. The ionization potential (IP) measures the difference between neutral state and core-ionized state at a particular atom in a molecule. The so-called chemical shift (CS) of the IP reflects the charge at, and in close vicinity of, the probed atom. Within the potential approximation, the CS can be directly converted into local charge ⁶.

In this paper we generalize the CS concept known from conventional, static XPS to electronically *excited* states, introducing the excited-state chemical shift (ESCS, not to be confused with the ESCS in nuclear magnetic resonance). We test this on the thionucleobase 2-thiouracil (2-tUra), which is photoexcited to a $\pi\pi^*$ state by an ultraviolet (UV) light pulse (Fig. 1). The S 2p photoionization with a soft x-ray pulse, of photon energy $h\nu$, leads to a photoelectron with kinetic energy $E_{\text{kin}}=h\nu-E_{\text{bind}}$. The molecular UV photoexcitation changes the local charge density at the probed atom (Fig. 1c), which leads to a specific ESCS. We find a direct relation between the ESCS and the local charge at the probe site in analogy to the potential model for the CS in static XPS ⁶. This allows one to circumvent complex calculations of IPs, while allowing for an interpretation based on chemical intuition. We show that the largest effect on the ESCS is due to electronic relaxation, especially if the local charge at the probed atom is grossly changed in the process. A smaller, but non-negligible effect, stems from geometry changes, which can also alter local charge at the probed atom.

Our studies extend existing theoretical ⁷⁻¹⁰ and experimental ¹¹⁻¹³ time-resolved (TR)-XPS by the demonstration of direct local charge recovery from ESCS. The x-ray typical element- and site-specific responses ^{14,15} are also accomplished using the now well-established time-resolved x-ray absorption spectroscopy (TR-XAS) method. In the soft x-ray range, TR-XAS has the capability to monitor electronic and nuclear dynamics ¹⁶⁻¹⁸, which has been demonstrated in ring-opening reactions ¹⁹, dissociation ²⁰, intersystem-crossing ²¹, ionization ²² as well as the interplay between $\pi\pi^*$ and $n\pi^*$ valence electronic states ^{23,24}. Hard x-ray absorption spectroscopy is highly sensitive to charge and spin states, however, only on metal atoms within molecules ^{25,26}. The novel TR-XPS extends this characteristic to lighter atoms and has the advantage that a fixed x-ray wavelength can be used to address several elements and sites. In addition, the use for molecules in thick solvent jets can also be accomplished by employing

harder x-rays for increased penetration depth of the radiation as well as escape depth of the photoelectrons for light-element XPS.

We demonstrate the new opportunities provided by TR-XPS on electronically excited states of a thionucleobase. Photoexcited thionucleobases are interesting because of efficient relaxation into long-lived triplet states (see Ref. ^{27,28} and references therein) triggering applications as photoinduced cross-linkers ^{29,30} and photoinduced cancer therapy ²⁸. Among those, 2-tUra is one of the most-studied cases on an ultrafast scale ²⁷, both experimentally, using transient absorption ³¹ and photoelectron spectroscopy ³¹⁻³³, and theoretically in static calculations ³⁴ and surface hopping trajectory simulations ^{35,36}. The model emerging from joint experimental-theoretical investigations includes ultrafast internal conversion from the photoexcited $S_2 \pi\pi^*$ state into the $S_1 n\pi^*$ state, followed by a sub-picosecond intersystem crossing ³². Relaxation from the triplet states to the ground state has previously been observed with a time constant of several ten picoseconds ³² while also indirect evidence for an ultrafast direct ground-state relaxation from the photoexcited state has been reported ³⁷.

The TR-XPS on electronically excited states allows us to identify the relaxation paths of 2-tUra by direct analysis of the ESCS and in addition comparisons to the calculated IPs of different states and geometries. Most interestingly, we identify a new ground state relaxation and a coherent electronic population oscillation modulating the sulphur 2p binding energy periodically, which has been predicted in time-dependent simulations ^{35,36}.

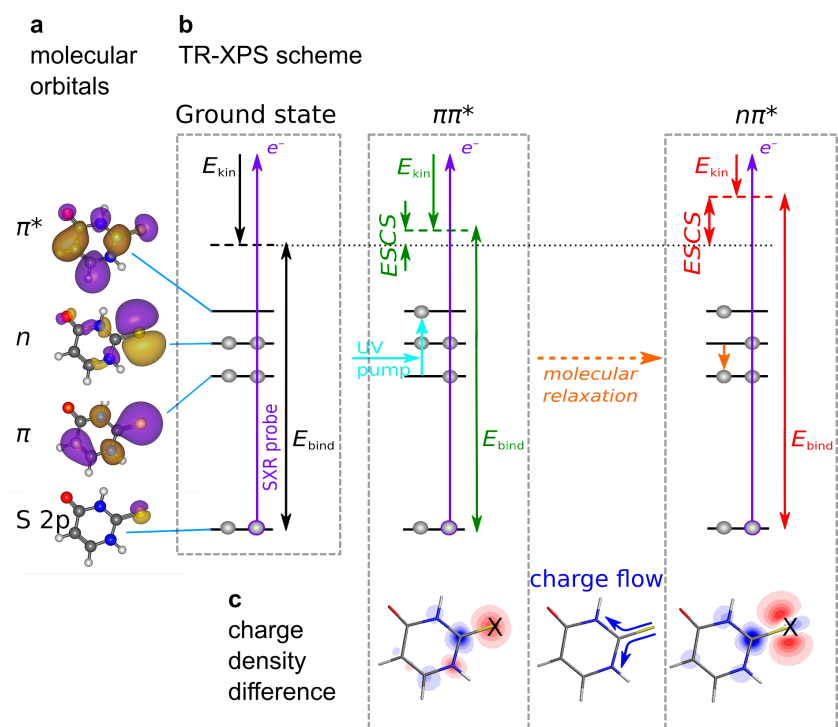


Figure 1: Schematic picture of TR-XPS and ESCS in 2-thiouracil in a molecular orbital representation. (a) Molecular valence (π , n , π^*) orbitals and a core (S 2p) orbital. (b) Probe of the sulphur 2p core level with a binding energy E_{bind} by means of a soft x-ray light pulse, leading to a photoelectron with a kinetic energy, E_{kin} . A UV pump pulse (cyan arrow) excites the 2-thiouracil from its electronic ground state (S_0) to a $\pi\pi^*$ state (S_2) which then relaxes further, for instance into the S_1 $n\pi^*$ state shown here. The difference in E_{bind} with respect to the ground state is the excited-state chemical shift ($ESCS = E_{\text{bind}}^{\text{excited state}} - E_{\text{bind}}^{\text{ground state}}$). (c) Difference in charge density between the ground state and the respective excited states (red: decreased electron density, blue: increased electron density). Increase in positive charge at the sulphur site (marked with X) increases E_{bind} and the ESCS.

Results

Difference spectra

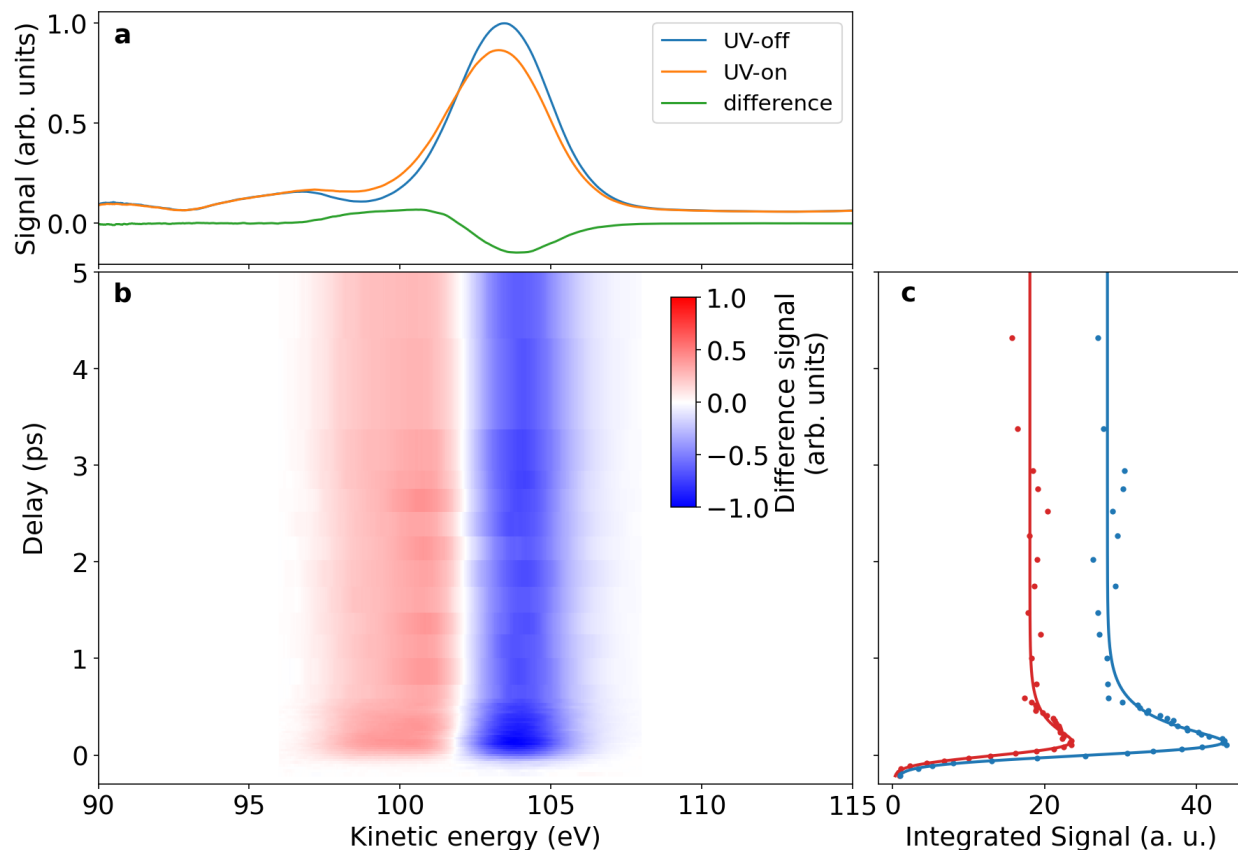


Figure 2: Experimental time-resolved XPS spectra of 2-thiouracil. (a) UV-on (orange) and UV-off (blue) photoelectron spectra as well as the difference spectrum (green) between UV-on and UV-off at a delay of 200 fs. (b) False-colour plot of time-dependent difference XPS with red indicating UV-induced increase of the photoelectron spectrum and blue a UV-induced decrease. (c) Integrated signal of the positive and negative parts of the difference spectra (dots) and fit to the data (solid line).

Figure 2a shows a photoelectron spectrum of 2-tUra obtained at the FLASH2 free-electron laser (FEL)³⁸ using a nominal photon energy of 272 eV and an average bandwidth of 1-2 %. The electron spectra are taken with a magnetic-bottle electron spectrometer (MBES). We identify the sulphur 2p-photoelectron line (blue) at a kinetic energy of 103.5 eV in agreement with the literature³⁹. The width of about 4 eV does prevent us from distinguishing the spin-orbit splitting^{39,40}. The photoelectron line is accompanied by shake-up satellites at around 91 and 96 eV⁴¹. Upon UV excitation (“UV-on”, orange line), the 2p-photoelectron line shifts towards lower kinetic energies. The difference spectrum (“UV-on” - “UV-off”, green line at a delay of 200 fs) is equal to the difference between ground-state (GS) and excited-state (ES) spectra times the fraction, f , of excited molecules ($f \cdot (ES - GS)$). Part of the main photoelectron line is shifted into the region of the upper shake-up satellite, but the main part of the satellite line at 96 eV and

the satellite at 91 eV remains unaffected. Figure 2b shows a time-dependent false-colour plot of the difference spectra. Temporal overlap has been determined by analysing the integrated absolute difference signal. The integrated signal under the positive/negative lobe in the difference spectrum is given in Figure 2c.

The difference feature keeps its characteristic lineshape over the timescale of our measurement shown in Fig. 2b, indicating a persistent kinetic energy shift to smaller values over the whole range. The difference-amplitude changes significantly during the first picosecond. We use an exponential model function convoluted with a Gaussian time-uncertainty function of 190 (± 10) fs FWHM (see Supplementary Discussion 1). We observe an exponential decay of 250 (± 20) fs to 75% of the maximal signal for the negative part and 220 (± 40) fs to 65% of the maximal signal for the positive part. The positive amplitude is always smaller than the negative amplitude. Systematic investigations of the difference spectra for various experimental settings exhibit the influence of so-called cyclotron resonances on the relative amplitudes in the MBES (see Supplementary Discussion 2). We therefore abstain from interpreting further the relative strength of the positive and negative features.

Spectral oscillations at small delays

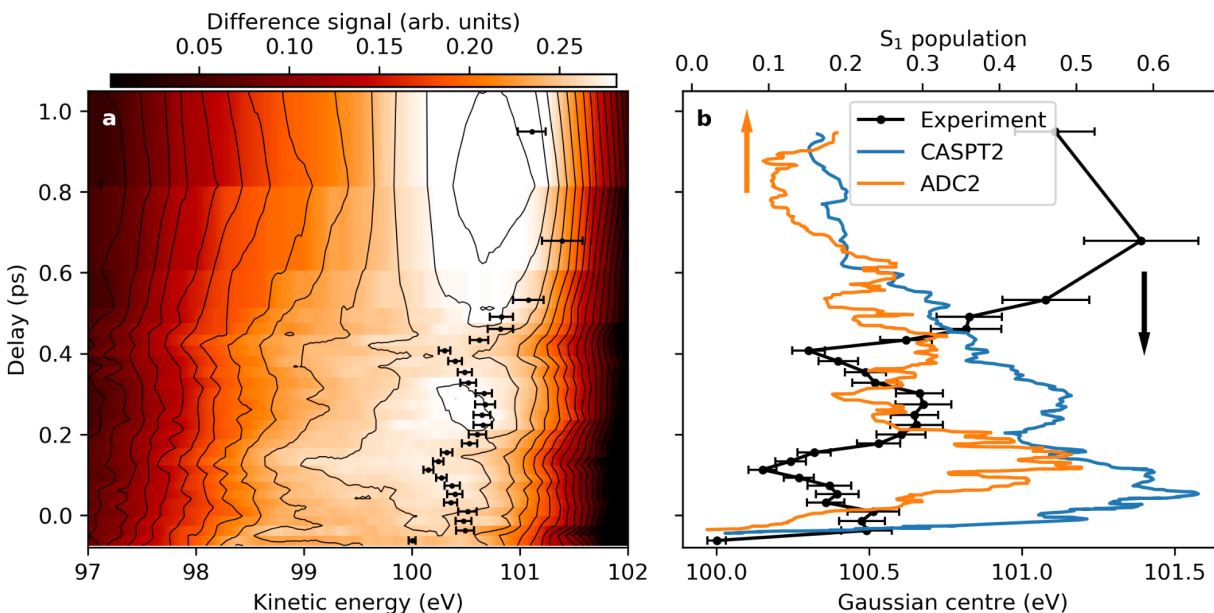


Figure 3: Experimental shifts and theoretical predictions on state population. a) False-colour contour plot of the positive lobe in Fig. 2b, normalized on the time-dependent area under the lobe. An oscillatory dynamics in the lineshape and position is visible for the first ~ 600 fs. At 150 fs and 400 fs delay, the spectrum is shifted to lower kinetic energy, while it is shifted to higher kinetic energies in between and afterwards. A Gaussian fit to the difference spectrum catches this trend in a few parameters. Shown here is the centre position of the lower kinetic energy Gaussian (black symbols with error bars). b) Comparison of the oscillation dynamics with trajectory simulations. The fitted Gaussian centre (black dots, bottom scale) for the positive lobe is compared with the population of the S_1 state, obtained from CASPT2 calculations of Ref. ³⁵

(blue line) and ADC(2) calculations of Ref. ³⁶(orange line, both on the top scale). The theoretical simulations do not include finite time-resolution and we shifted them by 50 fs to smaller delays to induce a transient rise of the signal around zero delay. The experimental 250 fs oscillation features have their counterparts in the simulated S_1 population, indicating the observation of a population exchange between the S_1 state and other electronic states.

Figure 3a shows a magnified part of the difference spectrum in Fig. 2b. In order to enhance the visibility of the spectral dynamics, we normalized each delay-slice on the area of the positive lobe. Despite the spectral width of about 4 eV, we identify oscillatory features in the positive part of the difference spectrum within the first ~600 fs. From zero delay to 150 fs, the spectrum shifts to lower kinetic energies and the peak of the spectrum widens. The shifts are most clearly visible in the spectral region from 99 to 101 eV. In the ground state, the shake-up peak at 96 eV has some spectral wing in this region. However, we do not observe a UV-induced change on the shake-up peak in its main part and lower energy wing. We thus assume that the main spectral effects in the 99 to 101 eV range are solely due to the UV-altered main photoelectron line.

After reaching minimal kinetic energies at 150 fs, the spectrum shifts towards higher kinetic energies by about 0.5 eV and the peak narrows reaching its extreme in the range between 200 to 300 fs. Subsequently, the spectrum shifts and widens again to reach its other extreme at 400 fs. For larger delays, the spectrum shifts again to higher kinetic energies. Further oscillations are not observed, however, for reasons of scarce experimental time, the delay steps are too coarse to follow additional oscillations. The negative lobe does not show systematic trends in this region and is therefore not shown in Fig. 3.

The simplest fitting model able to pick up the spectral fluctuations is a double Gaussian fit of the whole difference spectrum. While it might not be the best fit function, it is the simplest to quantify the spectral trends. Figure 3a displays the spectral position as well as the mean error as black symbols, with the 250 fs oscillation period clearly visible.

Difference spectra simulations

We will interpret the experimental results, casting them in the context of the rich literature on this molecule. Conclusions will also be drawn based on non-relativistic quantum chemical coupled-cluster calculations of the ground, valence-excited and core-ionised states of 2-tUra.

Previous calculations in the gas phase ³⁴ or in the presence of water solvent molecules ⁴² identified global, non-planar minima, as well as nearly planar minima, which can be potentially visited by the photoinduced wave packet.

Along the same lines, we optimised the geometry of the lowest valence singlet (S_0 , S_1 , S_2) and triplet (T_1 , T_2 , T_3) states with and without the constraint of planarity. Since the S_0 minimum is nearly planar, the excited state (unstable) planar minima are likely to play a role in the short time dynamics and are marked with an asterisk in Figs. 4 and 5. Fully-optimised, stable non-planar minima could be found for the S_1 , S_2 and T_1 states. The computational details are given in the Methods section and more extended in Supplementary Discussion 3.

For each optimised geometry and each valence state we calculated the binding energy of the electrons in the three 2p core orbitals of the S atom. We estimated the ionization cross sections

as proportional to the norm of the associated Dyson orbitals and used this data to simulate pump-probe photoelectron spectra at different geometries. The stick spectrum (shown in the Supplementary Discussion 4) was convoluted with a Gaussian of a FWHM of 3.5 eV, to match the width of the experimental bands.

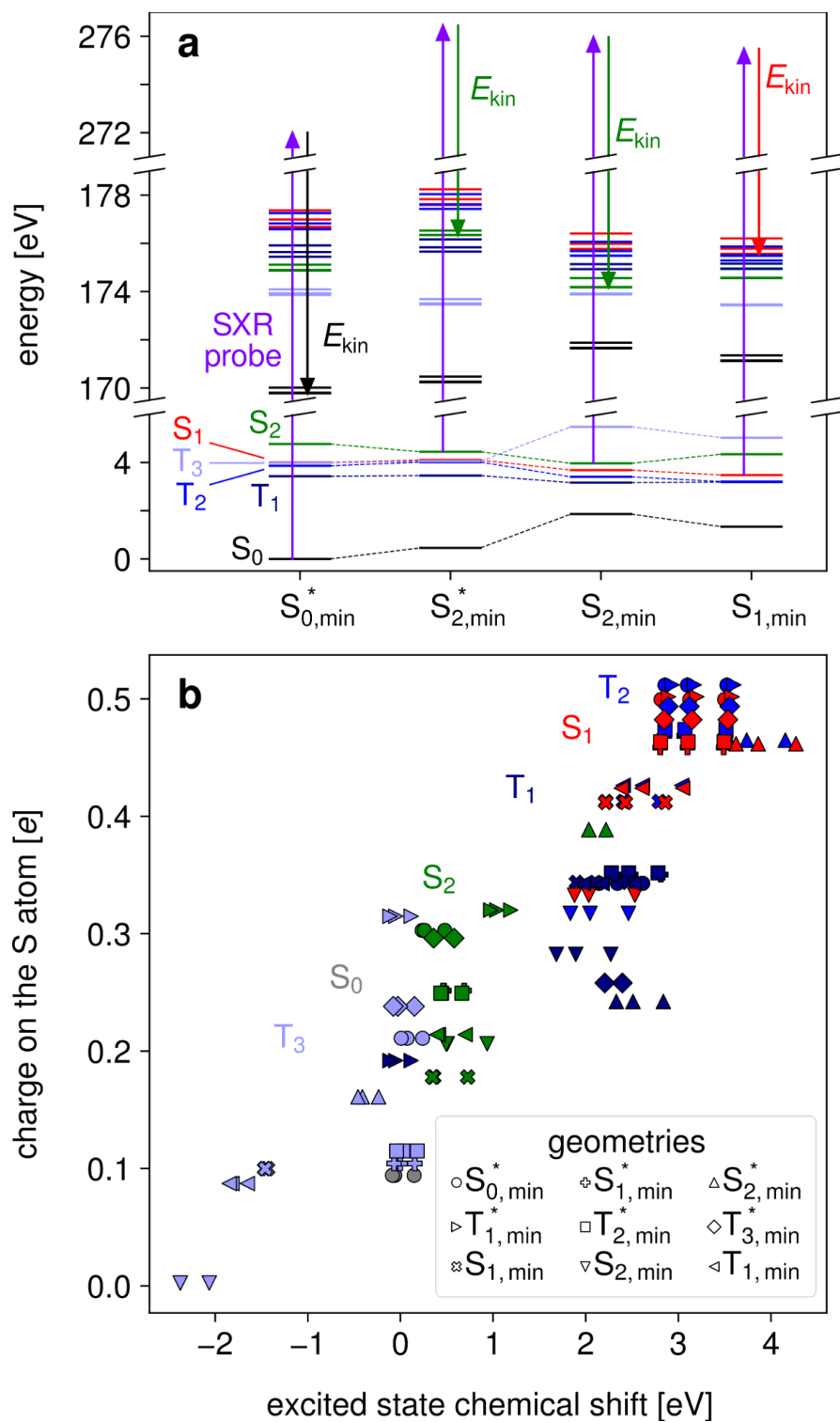


Figure 4: Soft x-ray photoelectron probing of the excited-state dynamics of 2-thiouracil in a multi-electron picture. (a) Calculated electronic energies of the valence excited states, in the

range 0-6 eV, and the core ionised states, in the range of 170-179 eV, for four geometries relevant in the short time dynamics. The arrows illustrate the $2p^{-1}$ ionisation process associated with the most intense transition. The core ionised states are grouped into sets of three states, which follow the colour coding of the valence states, meaning that their valence configuration is maintained with a $2p_x$, $2p_y$ or $2p_z$ core hole. Accordingly, the electron kinetic energy E_{kin} refers to ionisations out of S_0 , S_1 and S_2 , depending on the geometry. (b). Partial charges on the S atom are plotted against the binding energy of the 2p electrons, calculated for the valence states at nine different geometries. For each geometry, the graph includes three markers for each excited state (S_1 , S_2 , T_1 , T_2 , T_3); in addition, three dots are included for the ionisation from S_0 at $S_{0,min}^*$, for a total of $9 \times 3 \times 5 + 3 = 138$ markers. Asterisks denote restriction in the calculation of the states to planar geometries.

Discussion

We first discuss the experimental data without reference to the XPS simulations. The difference spectra of Figure 2, with their shift towards lower kinetic energies, indicate an increased E_{bind} of the UV excited states. The classical static XPS connects the E_{bind} of a particular element on a particular site within a molecule to the total charge at the probed atom, which is related to the electronegativity of the nearest neighbor atoms⁵. This connection is known as a ‘chemical shift’. Accordingly, we anticipate that the chemical shift can be generalized to a dynamic context as an excited-state chemical shift (ESCS) in form of the difference of excited and ground state binding energy. The long lasting shift of the kinetic energy would then indicate that the net effect of the photoexcitation is charge redistribution away from the sulphur atom (see Fig. 1). The electronic states inducing the strongest charge changes at the sulphur heteroatom are the $n\pi^*$ states. This is because the n (lone pair orbital) is strongly localized at the sulphur heteroatom and in the $n\pi^*$ states n is singly occupied with respect to double occupation in the electronic ground state. Overall this will lead to a strong ESCS to higher binding energies. The $^1n\pi^*$ state is generally considered a doorway state, leading from the UV excited $^1\pi\pi^*$ to the triplet states³⁷ and accordingly, we would expect an ESCS induced by this state.

The π orbitals are less localized at the sulphur atom. Intuitively removal of an electron from a π orbital would not induce as strong an ESCS as the n removal, but it will still lead to some ESCS. These relative strengths of the ESCS can also be estimated by a simple charge analysis of the molecular wavefunctions, a method that can even be implemented with simple Hartree-Fock orbitals. We performed a Löwdin-population-analysis on the wavefunctions of the different electronic states at different geometries, which yields partial charges on the atoms of the molecule. In Fig. 4b, the calculated partial charge on the S atom is plotted against the calculated ESCS, which we will not use in the discussion yet as it is a much more complex entity to calculate. We clearly identify the strongest local positive charge on the sulphur atom with respect to the ground states in the S_1 ($^1n\pi^*$) and T_2 ($^3n\pi^*$) states, confirming the intuitive arguments given above. The S_2 ($^1\pi\pi^*$) is characterized by a relatively low positive charge on the sulphur atom and the lowest T_1 ($^3\pi\pi^*$) state in its minimum geometry, generally considered as the long lasting state^{31,34}, is lying in between the $n\pi^*$ and S_2 ($^1\pi\pi^*$) states. Thus, the permanent ESCS to lower kinetic energies (higher binding energies) is consistent with a relaxation cascade

from the initially excited S_2 ($^1\pi\pi^*$) over the S_1 ($^1n\pi^*$) and possibly also T_2 ($^3n\pi^*$) states into the lowest T_1 ($^3\pi\pi^*$) state.

Closer inspection of the short-time dynamics in Fig. 3a provides extraordinary experimental details on the molecular relaxation dynamics. In the spectral shift dynamics, the strongest ESCS to lower kinetic energies (higher binding energies) is found at 150 and 400 fs, interrupted with an interval and followed by delays of smaller ESCS. Intuition based on the lone-pair orbital localization, as well as the simple local charge analysis at the sulphur atom mentioned above, indicate that this spectral shift reflects changes in the electronic state of the molecule with maximal $n\pi^*$ contributions at 150 and 400 fs and consequently minimal $n\pi^*$ contributions in between and after. We compare theoretical predictions of the S_1 ($^1n\pi^*$) state population dynamics from the trajectory surface-hopping calculations of Mai et al. ^{35,36} in Fig. 3b. The S_1 populations calculated using CASPT2 and ADC(2) potentials show indeed dynamics that fit well to the experimentally observed shifts. The oscillation period depends on the theoretical approach, and the timing of the second S_1 population maximum fits the experimental data better in the case of the ADC(2) approach. The simulations of Mai et al. predict a population transfer among the S_1 , S_2 and triplet states in a coherent fashion and the details of states participating in the population dynamics depends on the applied electronic structure method. However, in both cases, the S_1 state, having the highest IP of all states, carries the largest oscillation. This comparison strongly supports the experimental arguments for observing population dynamics entering and leaving the S_1 state in a coherently modulated fashion.

Similar coherent modulations have been observed in the transient spectra for 4-tUra and 2-tUra and in liquid phase ^{42,43}. In case of 4-tUra, much faster, sub-100 fs, coherent modulations have been observed in fs transient absorption spectra and attributed to particular vibrational modes in the electronically excited state of 4-tUra ⁴³. For the case of 2-tUra, the same experimental methods exhibit oscillations with a period very similar to ours ⁴², which is however not interpreted. We also checked the assignment to a purely vibrational coherence by performing a normal mode analysis at the calculated excited state minima. Only at the nonplanar minimum of the S_2 state we found a mode with a frequency of 131 cm^{-1} , thus compatible with a 250 fs modulation. However, this would mean that the molecular population should be dominated by the S_2 state for the 600 fs of our modulated time-interval, which is in contrast to all current literature suggestions. Also, for short times, we suggest that the molecule remains mostly planar on the S_2 state, as will be shown below by comparison to calculated difference spectra. Remarkably, valence photoelectron spectra of 2-tUra in the gas phase do not show these modulations ³¹, demonstrating that the ESCS in XPS is able to pick up molecular dynamics beyond reach for valence electron photoemission.

On top of the coherently modulated signal, we find an amplitude decay with a time-constant of 220-250 fs, being equal on the positive and negative lobe of the difference spectra within the error bars. Similar short decays have been observed in liquid and gas phase studies of 2-tUra. In valence photoelectron spectroscopy, a time constant of around 300 fs is observed for the excitation wavelength corresponding to the one used here ³¹. Based on the calculated valence ionization potentials of the different states ⁴⁴, the decay is attributed to relaxation from the S_1 ($^1n\pi^*$) to the triplet state manifold. Liquid-phase transient absorption spectra of 2-tUra in the same work show similar time constants and the same interpretation is applied ³¹. This is supported by a recent joint experimental-theoretical investigation that includes calculated

transient absorption windows at some of the molecule's crucial excited state positions⁴². The observed vanishing contrast in our TR-XPS might need to be interpreted in a different way than the $S_1(1n\pi^*)$ - triplet state relaxation, as we would expect to still observe a ESCS leading to different features in the triplet manifold. The state diminishing the modulation contrast of the difference spectra would have to show a small ESCS with respect to the ground state, and thus be electronically similar - or identical - to the ground state. We thus suggest an ultrafast molecular decay of part of the population into the electronic ground state and check it further by comparison to ESCS simulations below.

We now discuss the calculated ESCS and its connection to the charge on the sulphur atom in the photoexcited states. We observe the remarkable linear relation between binding energy and charge, closely resembling the potential model introduced in static XPS⁶. While many effects such as final-state charge relaxation and core-hole screening^{13,45} shape the calculated binding energy, the linear trend prevails. This provides a generalized concept for deducing local charge changes in electronically excited states from the ESCS. Further well-established corrections known from static XPS to this plot make the E_{bind} - charge connection even more obvious (Supplementary discussion 5).

In addition, we can clearly distinguish drivers behind the charge and ESCS shifts. The colours in Fig. 4 indicate the electronic state while the different symbols indicate geometries, corresponding to minima or saddle points on different potential energy surfaces. We clearly observe clustering according to electronic state, although very widely differing geometries have been used. Thus the main factor for local charge and therefore binding energy is the electronic state of the molecule. This in turn gives core-level photoelectron spectroscopy high electronic state sensitivity. The exceptions of one S_2 and T_1 geometry are explained in the Supplementary Discussion 6. The data for the S_1 and T_2 states are very well clustered in the upper right corner of Fig. 4b, with the highest IP. As explained above, these states have $n\pi^*$ character and possess a high positive charge on the sulphur atom, which is also illustrated in Fig. 1.

In Fig. 5, we assess details of the TR-XPS spectra by comparison with the calculated spectra, extending our discussion of the purely experimental features. The onset of the experimental difference feature around time-zero is shown in more detail in the waterfall plot of Fig. 5a. The difference signal gets stronger with delay indicating an increasing f over the time-resolution of 191 fs. We initially identify the development of the negative feature sitting stable at 104 eV and a comparatively broader positive feature at lower kinetic energies. According to model and intuition, this should belong to electronic states with higher positive charge on the sulphur atom.

We continue discussing the picosecond difference spectra, comparing them to calculated difference spectra in Fig. 5b and c. Among the states with highest local charge and thus highest E_{bind} are the S_1 , T_1 and T_2 states. The unstable, restricted planar minima/saddle points of S_1 and T_2 (Fig. 5c) could be responsible for parts of the difference spectra for a limited time until relaxation into a non-planar geometry. Among these non-planar geometries, both the S_1 and T_1 show agreement with the experimental difference spectra (Fig. 5b). The missing low-energy wing from 97-98.5 eV in the theoretical spectra can likely be attributed to the fact that we

neglect wave-packet and incoherent thermal distribution effects resulting in extended geometry coverage. The shake-up phenomena are also not modelled. However we do not observe a change of the shake-up peaks and we would expect that the observation of UV-induced effects on the weaker satellite lines requires better signal-to-noise. The theoretical simulations strengthen the arguments given in the context of Fig. 3, showing that a strong ESCS due to the S_1 coherent dynamics is followed by a state with less ESCS. We note that simulations/experiments on the pyrimidine nucleobases call for the S_1 $^1n\pi^*$ state to be occupied first after S_2 relaxation⁴⁶. Only thereafter will the triplet states gain population. Based on the experimental features, we can exclude the planar geometries of the T_1 and T_3 states to play a major role in the relaxation process. A comparison to the ESCS in Fig. 4b implies that the charge at the sulphur atom has reached about half a positive value due to the molecular relaxation.

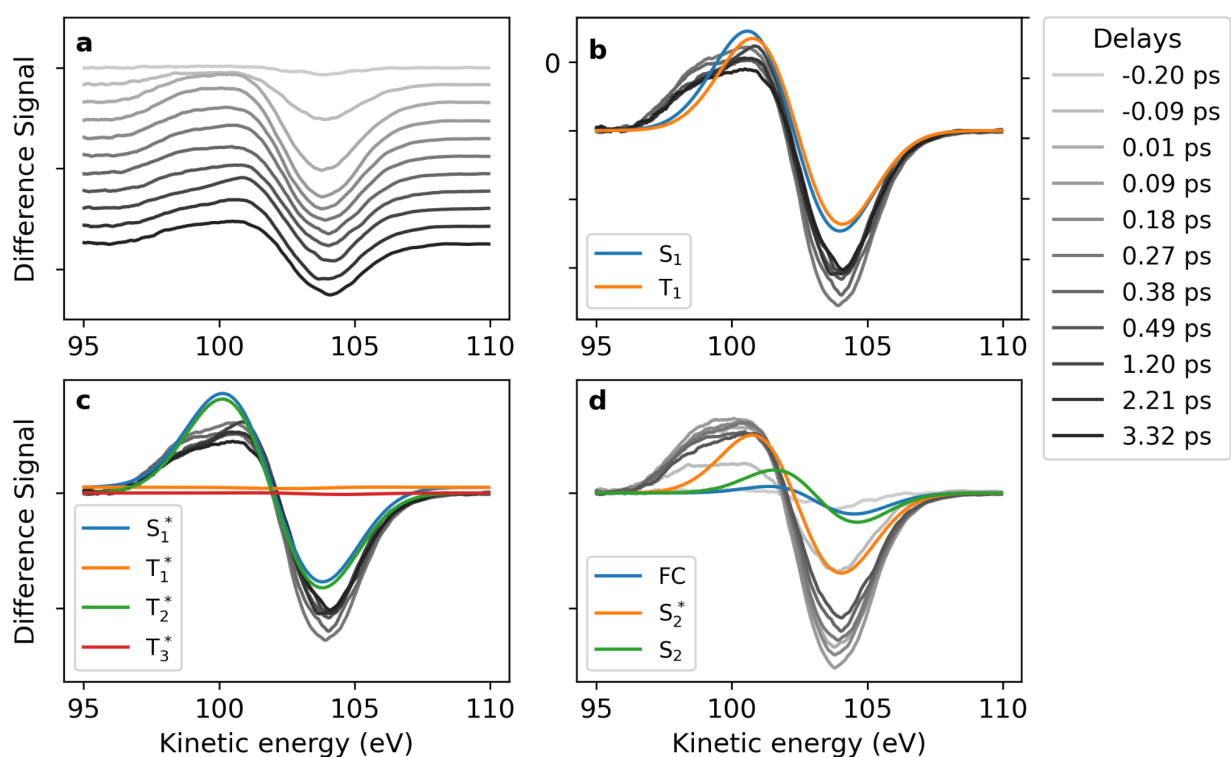


Figure 5: (a) Ridgeline plot of experimental difference spectra for different pump-probe delays between -0.2 to 3.32 ps. (b - d) Comparison of experiment (greyscale lines) with theoretical (coloured lines) difference spectra computed at the coupled-cluster level of theory. All calculated difference spectra are shifted lower in kinetic energy by 1.3 eV. (b) and (c) Spectra with delays in the range 0.27 to 3.32 ps, (d) spectra with delays -0.2 to 0.49 ps. The theoretical spectra use the energies at the minima (S_2 is the nonplanar, S_2^* is the restricted geometry) and the Frank-Condon geometry. Asterisks denote restriction in the calculation of the states to planar geometries.

We now return to the initial 220-250 fs decay of the difference feature, which can be an indication of relaxation of the charge back to the ground state distribution, into states with negligible photoionisation cross section, or into states with an IP equal to the electronic ground state before photoexcitation. To obtain more insight, we compare the experimental XPS to simulations in Fig. 5b-d. Figure 5d shows the S_2 state difference spectra in three different molecular geometries. Figure 5c shows spectra with 'unstable' planar geometries. The most important is the S_1 state, others are expected to play a minor role in the dynamics for short times^{35,36}. Figure 5b shows difference spectra for the S_1 and T_1 states at their respective potential energy minimum geometry. The unstable T_1^* and T_3^* spectra are indeed flat on our scale and could in principle explain the observed decay in difference amplitude. However, these geometries cannot be stable, and cannot explain the long-lasting reduction in amplitude with the 220-250 fs exponential decay. In addition, the remaining calculated non-flat difference spectra do not exhibit a large enough difference. We therefore attribute the observed decay to an ultrafast relaxation into the electronic ground state with net zero charge change with a 220-250 fs time-constant.

Ground-state relaxation has been discussed before in the solution as well as in the gas phase^{37,47,31}. In earlier solution-phase work, a remark on an incomplete triplet yield could be interpreted in favour of an ultrafast ground state decay channel³⁷. More recent work in the gas phase has attributed time-constants from 50 to 200 ps to ground state relaxation³¹. Our ground state channel is close to the 300 fs decay observed in Ref.³¹ which was attributed to intersystem crossing previously.

We now compare early difference spectra to the calculated spectra of the directly photoexcited S_2 state in different geometries in Fig. 5d. The best representation is given by the S_2^* planar geometry. The Franck-Condon spectrum should be included in the difference spectra, however, the short lifetime of this point as compared to our time-resolution makes it a minor contributor. We can, however, exclude a relaxation with major contributions from the S_2 out-of-plane minimum (green line), as this would mean a shift in the zero-crossing feature by about 1 eV to higher kinetic energies, which is not observed in the experiment. This observation agrees with the predictions of trajectory calculations when using a CASPT2 approach to electronic structure³⁵ but is in contrast to trajectory calculations with an ADC(2) electronic structure approach³⁶. While in the first reference the S_2 lifetime is below 100 fs and thus too short for the molecule to effectively reach out of plane geometries, the latter predicts an S_2 lifetime of 250 fs which allows for out of plane geometries.

In a recent theoretical-experimental solution phase study, two $^1\pi\pi^*$ states with a slight energy gap are assumed to be populated and while the upper one is predicted to relax via out-of-plane geometries, the lower one is suggested to relax via planar geometries⁴². We find that our calculated geometries are very similar to the ones from Ref.⁴² (see the Supplementary Discussion 3 for a full comparison) and thus our analysis above would clearly advocate for initial planar geometries in the relaxation path. However, as our study is performed on isolated

molecules instead of in solution phase it is not clear if we have any appreciable admixture of the higher lying $1\pi\pi^*$ state.

Conclusion

We have introduced the concept of excited-state chemical shift (ESCS) in TR-XPS and shown that this powerful concept can be applied to deduce charge distribution changes in excited molecules. We observe rich dynamics on a sub-ps timescale. Based on intuitive arguments, we can assign the spectral features to coherent population exchange of the $n\pi^*$ state, inducing a strong ESCS, with other electronic states of less ESCS. In addition, we identify an ultrafast ground state relaxation path based on decaying amplitude in the differential signal. The calculated ESCS as a function of electronic state and geometry help in interpreting the geometric changes of the molecule after UV excitation in terms of a planar relaxation path on the photoexcited $1\pi\pi^*$ state. The connection between charge change at the probe site and the exactly calculated ESCS can be well approximated by a potential model, as in ground state XPS. This will provide a methodological basis for an intuitive understanding of charge dynamics in photoexcited isolated molecules on the femto- and attosecond time scale but also for photocatalytic systems. In a next step, one can address more than one site of the molecule using TR-XPS and map the charge flow induced by photoexcitation over the whole molecule.

Methods

Time-resolved UV pump soft x-ray probe (photo-) electron spectroscopy: The experiment was performed at the FL24 beamline of the FLASH2 facility at DESY using the newly built URSA-PQ apparatus. A detailed description of the apparatus and the experiment can be found elsewhere^{48,49}. In short, the apparatus includes a magnetic bottle time-of-flight electron spectrometer (MBES), a capillary oven to evaporate the 2-thiouracil samples at 150°C and a paddle with beam diagnostics on top of the oven. UV pump pulses of 269 nm center wavelength, 80 fs duration and an energy below 1 μ J were focused to a 50 μ m focus to pre-excite the molecules into the $\pi\pi^*$ state. Power scans on the time-dependent spectral features were performed to assure that the signal is not over-pumped by the UV pulses (Supplementary Discussion 7).

Tunable soft x-ray pump pulses were produced in form of SASE (self-amplified spontaneous emission) radiation. Every second x-ray pulse was delivered without UV excitation for obtaining a reference on the non-excited molecule. The mean x-ray photon energy was set to 272 eV with a bandwidth of 1-2 % (including jitter). The x-ray probe was linearly polarised parallel to the axis of the magnetic bottle spectrometer and the UV polarization. The focal size of the x-ray beam was slightly larger than the UV spot size. Systematic power scans were performed to exclude nonlinear effects in the x-ray induced electron spectra (see SI). To increase energy resolution of the spectrometer, the speed of the ejected electrons was reduced by an -80 V retardation voltage on an electrostatic lens in front of the 1.7 m long flight tube which was kept at a constant potential. The energy resolving power of the MBES ($E/\Delta E$) has been determined with Kr MNN Auger lines to be 40 at 0 V retardation. Based on the sulphur 2p photoelectron line, we estimate the resolution to be better than 30 with respect to the total kinetic energy. The time-dependent spectra were measured for a series of delays. In each scan, the delays were set randomly to

avoid systematic effects. We measure the difference spectra of UV excited to non-excited shots. The data evaluation is described in Supplementary Discussion 8.

Theoretical calculations: The geometry optimization of ground state 2-thiouracil was performed using coupled-cluster theory with singles and doubles (CCSD) with the 6-311++G** basis set^{50,51}. Valence excited state optimizations and energy calculations at specific geometries were performed using the equation-of-motion formalism (EOM-CCSD) with the same basis set. All calculations were performed using the package Q-Chem 4.4⁵². At all computed geometries the valence excited states' wavefunctions are dominated by a singly-excited configuration. For the states S_1 , T_2 ($n\pi^*$) and S_2 , T_1 ($\pi\pi^*$) the involved orbitals at the Franck-Condon point are shown in Fig. 1. The structural parameters of the optimised planar and non-planar geometries on the different electronic states are reported in the Supplementary Discussion 3.

The binding energy of the electrons in the 2p orbitals of the sulphur atom were calculated using the equation-of-motion coupled-cluster method for IPs (EOM-IP-CCSD)⁵³ with the 6-311++G** basis set for the S atom and the 6-31++G basis for all other atoms. Photoelectron intensities were approximated as the geometric mean of the norms of the left and right Dyson orbitals associated with the ionization process¹⁰. The target core-excited states of the cation were identified as the eigenstates which have the largest overlap with initial guess states, obtained by applying the annihilation operator of the three 2p electrons on reference CCSD wavefunctions, according to the procedure implemented in Q-Chem. To this end, reference CCSD wavefunctions for the different electronic states of the neutral molecule were calculated starting from unrestricted Hartree-Fock wavefunctions, which were optimised using the maximum overlap method (MOM), in order to mimic the (singly excited) orbital occupancy of the excited states. A similar strategy has been recently validated by Coriani and coworkers to model pump-probe x-ray absorption spectra of nucleobases at the coupled cluster level⁵⁴. Spin-orbit coupling, leading to a splitting of the core-ionised states of the order of 1 eV (not resolved due to spectral broadening) is not included in the calculations.

Acknowledgements

We thank the Volkswagen foundation for funding via a Lichtenberg Professorship.

We thank the BMBF for funding the URSA-PQ apparatus and for funding JM via Verbundforschungsproject 05K16IP1. We acknowledge DFG funding via Grants GU 1478/1-1 (MG) and SA547/17-1 (PS). TJAW was supported by the US Department of Energy, Office of Science, Basic Energy Sciences, Chemical Sciences, Geosciences, and Biosciences Division. RF thanks the Swedish Research Council (VR) and the Knut and Alice Wallenberg Foundation, Sweden, for financial support. We acknowledge DESY (Hamburg, Germany), a member of the Helmholtz Association HGF, for the provision of experimental facilities. Part of this research was carried out at FLASH2. FC acknowledges support from the European Research Council under the ERC-2014-StG STARLIGHT (Grant Agreement No. 637756).

References

1. Domcke, W., Yarkony, D. R. & Köppel, H. *Conical intersections electronic structure, dynamics and spectroscopy*. (World Scientific Publishing Company, 2011).
2. Levine, B. G. & Martínez, T. J. Isomerization Through Conical Intersections. *Ann. Rev. Phys. Chem.* **58**, 613–634 (2007).
3. Weinberg, D. R. *et al.* Proton-Coupled Electron Transfer. *Chem. Rev.* **112**, 4016–4093 (2012).
4. Haining Tian, Gerrit Boschloo, & Anders Hagfeldt. *Molecular devices for solar energy conversion and storage*. (Springer Berlin Heidelberg, 2017).
5. Siegbahn, K. *ESCA applied to free molecules*. (North-Holland Pub. Co, 1969).
6. Gelius, U. Binding Energies and Chemical Shifts in ESCA. *Phys. Scr.* **9**, 133–147 (1974).
7. Bennett, K., Kowalewski, M. & Mukamel, S. Nonadiabatic Dynamics May Be Probed through Electronic Coherence in Time-Resolved Photoelectron Spectroscopy. *J. Chem. Theory Comput.* **12**, 740–752 (2016).
8. Neville, S. P., Chergui, M., Stolow, A. & Schuurman, M. S. Ultrafast X-Ray Spectroscopy of Conical Intersections. *Phys. Rev. Lett.* **120**, 243001 (2018).
9. Inhester, L., Li, Z., Zhu, X., Medvedev, N. & Wolf, T. J. A. Spectroscopic Signature of Chemical Bond Dissociation Revealed by Calculated Core-Electron Spectra. *J. Phys. Chem. Lett.* **10**, 6536–6544 (2019).
10. Vidal, M. L., Krylov, A. I. & Coriani, S. Dyson orbitals within the fc-CVS-EOM-CCSD framework: theory and application to X-ray photoelectron spectroscopy of ground and excited states. *Phys. Chem. Chem. Phys.* **22**, 2693–2703 (2020).
11. Siefertmann, K. R. *et al.* Atomic-Scale Perspective of Ultrafast Charge Transfer at a Dye–Semiconductor Interface. *J. Phys. Chem. Lett.* **5**, 2753–2759 (2014).
12. Brauße, F. *et al.* Time-resolved inner-shell photoelectron spectroscopy: From a bound molecule to an isolated atom. *Phys. Rev. A* **97**, 043429 (2018).
13. Leitner, T. *et al.* Time-resolved electron spectroscopy for chemical analysis of photodissociation: Photoelectron spectra of $\text{Fe}(\text{CO})_5$, $\text{Fe}(\text{CO})_4$, and $\text{Fe}(\text{CO})_3$. *J. Chem. Phys.* **149**, 044307 (2018).
14. Bergmann, U., Yachandra, V. & Yano, J. *X-Ray Free Electron Lasers: Applications in Materials, Chemistry and Biology*. (Royal Society of Chemistry, 2017).
15. Young, L. *et al.* Roadmap of ultrafast x-ray atomic and molecular physics. *J. Phys. B: At. Mol. Opt. Phys.* **51**, 032003 (2018).
16. Neville, S. P. *et al.* Beyond structure: ultrafast X-ray absorption spectroscopy as a probe of non-adiabatic wavepacket dynamics. *Faraday Discuss.* **194**, 117–145 (2016).
17. Neville, S. P. *et al.* Excited state X-ray absorption spectroscopy: Probing both electronic and structural dynamics. *J. Chem. Phys.* **145**, 144307 (2016).
18. Segatta, F. *et al.* Exploring the capabilities of optical pump X-ray probe NEXAFS spectroscopy to track photo-induced dynamics mediated by conical intersections. *Faraday Discuss.* **221**, 245–264 (2020).
19. Attar, A. R. *et al.* Femtosecond x-ray spectroscopy of an electrocyclic ring-opening reaction. *Science* **356**, 54–59 (2017).
20. Pertot, Y. *et al.* Time-resolved x-ray absorption spectroscopy with a water window high-harmonic source. *Science* **355**, 264–267 (2017).

21. Bhattacharjee, A., Pemmaraju, C. D., Schnorr, K., Attar, A. R. & Leone, S. R. Ultrafast Intersystem Crossing in Acetylacetone via Femtosecond X-ray Transient Absorption at the Carbon K-Edge. *J. Am. Chem. Soc.* **139**, 16576–16583 (2017).
22. Loh, Z.-H. *et al.* Observation of the fastest chemical processes in the radiolysis of water. *Science* **367**, 179–182 (2020).
23. Wolf, T. J. A. *et al.* Probing ultrafast $\pi\pi^*/n\pi^*$ internal conversion in organic chromophores via K-edge resonant absorption. *Nature Comm.* **8**, 29 (2017).
24. Ehlert, C., Gühr, M. & Saalfrank, P. An efficient first principles method for molecular pump-probe NEXAFS spectra: Application to thymine and azobenzene. *J. Chem. Phys.* **149**, 144112 (2018).
25. Bressler, C. & Chergui, M. Ultrafast X-ray Absorption Spectroscopy. *Chem. Rev.* **104**, 1781–1812 (2004).
26. Zhang, W. *et al.* Tracking excited-state charge and spin dynamics in iron coordination complexes. *Nature* **509**, 345–348 (2014).
27. Arslançan, S., Martínez-Fernández, L. & Corral, I. Photophysics and Photochemistry of Canonical Nucleobases' Thioanalogs: From Quantum Mechanical Studies to Time Resolved Experiments. *Molecules* **22**, 998 (2017).
28. Ashwood, B., Pollum, M. & Crespo-Hernández, C. E. Photochemical and Photodynamical Properties of Sulfur-Substituted Nucleic Acid Bases,. *Photochem. Photobiol.* **95**, 33–58 (2019).
29. Zhang, X. *et al.* Novel DNA lesions generated by the interaction between therapeutic thiopurines and UVA light. *DNA Repair* **6**, 344–354 (2007).
30. Brem, R., Daehn, I. & Karran, P. Efficient DNA interstrand crosslinking by 6-thioguanine and UVA radiation. *DNA Repair* **10**, 869–876 (2011).
31. Sánchez-Rodríguez, J. A. *et al.* 2-Thiouracil intersystem crossing photodynamics studied by wavelength-dependent photoelectron and transient absorption spectroscopies. *Phys. Chem. Chem. Phys.* **19**, 19756–19766 (2017).
32. Mohamadzade, A., Bai, S., Barbatti, M. & Ullrich, S. Intersystem crossing dynamics in singly substituted thiouracil studied by time-resolved photoelectron spectroscopy: Micro-environmental effects due to sulfur position. *Chem. Phys.* **515**, 572–579 (2018).
33. Mai, S., Mohamadzade, A., Marquetand, P., González, L. & Ullrich, S. Simulated and Experimental Time-Resolved Photoelectron Spectra of the Intersystem Crossing Dynamics in 2-Thiouracil. *Molecules* **23**, 2836 (2018).
34. Mai, S., Marquetand, P. & González, L. A Static Picture of the Relaxation and Intersystem Crossing Mechanisms of Photoexcited 2-Thiouracil. *J. Phys. Chem. A* **119**, 9524–9533 (2015).
35. Mai, S., Marquetand, P. & González, L. Intersystem Crossing Pathways in the Noncanonical Nucleobase 2-Thiouracil: A Time-Dependent Picture. *J. Phys. Chem. Lett.* **7**, 1978–1983 (2016).
36. Mai, S. *et al.* Surface hopping dynamics including intersystem crossing using the algebraic diagrammatic construction method. *J. Chem. Phys.* **147**, 184109 (2017).
37. Pollum, M. & Crespo-Hernández, C. E. Communication: The dark singlet state as a doorway state in the ultrafast and efficient intersystem crossing dynamics in 2-thiothymine and 2-thiouracil. *J. Chem. Phys.* **140**, 071101 (2014).

38. Faatz, B. *et al.* Simultaneous operation of two soft x-ray free-electron lasers driven by one linear accelerator. *New J. Phys.* **18**, 062002 (2016).
39. Giuliano, B. M. *et al.* Tautomerism in 4-Hydroxypyrimidine, S -Methyl-2-thiouracil, and 2-Thiouracil. *J. Phys. Chem. A* **114**, 12725–12730 (2010).
40. Plekan, O. *et al.* Functionalisation and immobilisation of an Au(110) surface via uracil and 2-thiouracil anchored layer. *Phys. Chem. Chem. Phys.* **17**, 15181–15192 (2015).
41. Föhlisch, A. *et al.* Direct observation of electron dynamics in the attosecond domain. *Nature* **436**, 373–376 (2005).
42. Teles-Ferreira, D. C. *et al.* A Unified Experimental/Theoretical Description of the Ultrafast Photophysics of Single and Double Thionated Uracils. *Chem. Eur. J.* **26**, 336–343 (2020).
43. Borrego-Varillas, R. *et al.* Observation of the Sub-100 Femtosecond Population of a Dark State in a Thiobase Mediating Intersystem Crossing. *Journal of the American Chemical Society* **140**, 16087–16093 (2018).
44. Ruckenbauer, M., Mai, S., Marquetand, P. & González, L. Photoelectron spectra of 2-thiouracil, 4-thiouracil, and 2,4-dithiouracil. *J. Chem. Phys.* **144**, 074303 (2016).
45. Mårtensson, N. & Nilsson, A. On the origin of core-level binding energy shifts. *J. Electr. Spectr. Rel. Phen.* **75**, 209–223 (1995).
46. Improta, R., Santoro, F. & Blancafort, L. Quantum Mechanical Studies on the Photophysics and the Photochemistry of Nucleic Acids and Nucleobases. *Chem. Rev.* **116**, 3540–3593 (2016).
47. Yu, H. *et al.* Internal conversion and intersystem crossing pathways in UV excited, isolated uracils and their implications in prebiotic chemistry. *Phys. Chem. Chem. Phys.* **18**, 20168–20176 (2016).
48. Metje, J. *et al.* URSA-PQ: A Mobile and Flexible Pump-Probe Instrument for Gas Phase Samples at the FLASH Free Electron Laser. *Applied Sciences* **10**, 7882 (2020).
49. Lever, F. *et al.* Ultrafast dynamics of 2-thiouracil investigated by time-resolved Auger spectroscopy. *J. Phys. B: At. Mol. Opt. Phys.* **54**, 014002 (2020).
50. Shavitt, I. & Bartlett, R. J. *Many – Body Methods in Chemistry and Physics: MBPT and Coupled-Cluster Theory.* (Cambridge University Press, 2009).
51. Bartlett, R. J. & Musiał, M. Coupled-cluster theory in quantum chemistry. *Rev. Mod. Phys.* **79**, 291–352 (2007).
52. Shao, Y. *et al.* Advances in molecular quantum chemistry contained in the Q-Chem 4 program package. *Mol. Phys.* **113**, 184–215 (2015).
53. Krylov, A. I. Equation-of-Motion Coupled-Cluster Methods for Open-Shell and Electronically Excited Species: The Hitchhiker’s Guide to Fock Space. *Annu. Rev. Phys. Chem.* **59**, 433–462 (2008).
54. Tsuru, S. *et al.* An assessment of different electronic structure approaches for modeling time-resolved x-ray absorption spectroscopy. *Struct. Dyn.* **8**, 024101 (2021).

Supplemental information

1 Fits of the delay-dependent signals

The integral of the difference signal and the amplitudes from the double Gaussian fit show similar delay-dependent behaviour and have thus been fitted with the same function:

$$S(t) = \sum_{i=1}^2 A_i \cdot \exp\{-\tau_i^{-1} \cdot (t - t_0)\} \exp\{0.5 \cdot \tau_i^{-2} \cdot \sigma^2\} \left[1 + \operatorname{erf}\left(\frac{t-t_0-\tau_i^{-1} \cdot \sigma^2}{\sqrt{2}\sigma}\right) \right] \quad (1)$$

The equation represents a Gaussian time-uncertainty function convoluted with two exponential decays. Here, A_i and τ_i are the amplitude and decay constant of the i -th component. t_0 is the time-zero, i.e. the overlap between pump and probe pulse, and σ describes the temporal resolution (with σ^2 being the variance of the Gaussian function). The erf is the Gauss error function. The fitting range was restricted to -0.2 to +10 ps.

First, the integral of the absolute difference signal ($S_{\text{int}}^{\text{abs}}$) was fitted. The fitted t_0 value was used to correct the delays. Then, the integral of the positive (S_{int}^+) and negative (S_{int}^-) contributions to the difference spectra as well as the amplitudes from the Gaussian fits (S_{amp}^{\pm}) were fitted with a fixed time uncertainty using the value from $S_{\text{int}}^{\text{abs}}$. The results of all five fits are summarised in table S1.

The full width at half maximum of the Gaussian time-uncertainty function is 190 ± 10 fs. This value includes the pulse duration of the UV pump and the x-ray probe pulse as well as temporal jitter^{1,2}. The time constant of the first decay component τ_1 lies between 200 and 300 fs for all fits with an average value of 235 ± 10 fs. For the second decay constant τ_2 , only two fits give values within the picosecond range (~ 200 ps). The other values are within nano- or even microsecond range with similarly large fitting errors (noted with >1000 in table S1). Increasing the delay range for the fit does not improve the values for τ_2 . The values for τ_1 stay similar. A normalized plot in Fig. S1, allowing for a better comparison of the positive and negative signal decay, confirms that the observed decays on the positive and negative lobe are equal.

Table S1: Fitted parameters of delay dependent amplitudes and integrals. * after correcting the delays with value from $S_{\text{int}}^{\text{abs}}$. “-” indicates that value from $S_{\text{int}}^{\text{abs}}$ has been used.

	$S_{\text{int}}^{\text{abs}}$	S_{int}^-	S_{int}^+	S_{amp}^-	S_{amp}^+
σ / fs	81 ± 5	-	-	-	-
t_0 / fs	-56 ± 4	$2.0 \pm 4.0^*$	$-6 \pm 6^*$	$1.5 \pm 3.0^*$	$5 \pm 4^*$
Amp 1	43 ± 4	31 ± 2	12 ± 2	10.4 ± 0.9	4.0 ± 0.4
τ_1 / fs	225 ± 30	250 ± 20	220 ± 40	210 ± 40	290 ± 60
Amp 2	46.5 ± 2	28.2 ± 0.8	17.5 ± 0.6	11.3 ± 0.40	5.2 ± 0.2
τ_2 / ps	200 ± 140	>1000	>1000	140 ± 140	>1000
offset	1.8 ± 1.0	1.0 ± 0.6	0.70 ± 0.6	0.51 ± 0.07	-0.07 ± 0.05

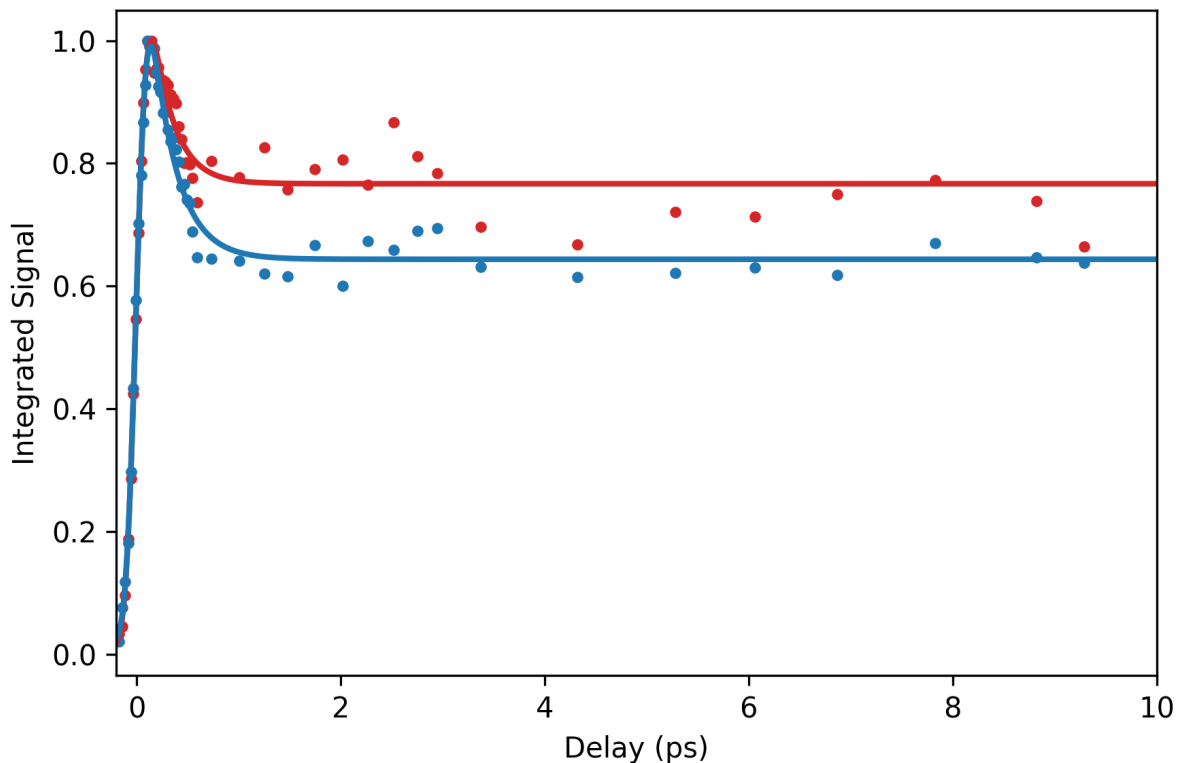


Figure S1: Integrated (absolute) signal for positive (red) and negative lobe (blue) of the S2p difference spectrum normalized on the maximum.

2 Magnetic bottle sensitivity

The data shown in the following plots (Fig. S2 to S4) were recorded on a follow up beamtime to investigate the influence of different experimental parameters on the photoelectron spectra. In Fig. S2, the solenoid (coil) current and thus the magnetic field inside the flight tube was changed. The electron spectra were recorded with a photon energy of 272 eV at a delay of 200 ps and a retardation voltage of -80 V. Panel a) shows the normalised difference spectra of the sulphur 2p photoline. The positive (red) and negative (blue) contributions broaden with increasing magnetic field and also shift towards lower kinetic energy. Additionally, panel b) shows the integrals of the positive and negative contributions of the spectra. The two lobes change signal strength in a counter-oscillatory way. Especially the negative lobe is stronger than the positive one at 200 mA which was the value also used for the data presented in this paper. In Fig. S3, the coil current was kept constant at 200 mA and instead the retardation voltage was scanned across -80 V, while the kinetic energy is corrected for the change in retardation potential. Again, panel a) shows the difference spectra and b) the integrals of the positive and negative contributions. The counter-oscillation of the two lobe integrals is again observed. This is also the case for a photon energy scan around 272 eV shown in Fig. S4 where the coil current and retardation voltage are kept constant at values of 200 mA and -80 V, respectively. Our systematic investigations of the difference spectra for various experimental settings exhibit the influence of cyclotron resonances on the relative amplitudes in the MBES, an aspect which

is well known for this kind of electron spectrometer³. In future runs, the characterisation might be used to calibrate the MBES sensitivity.

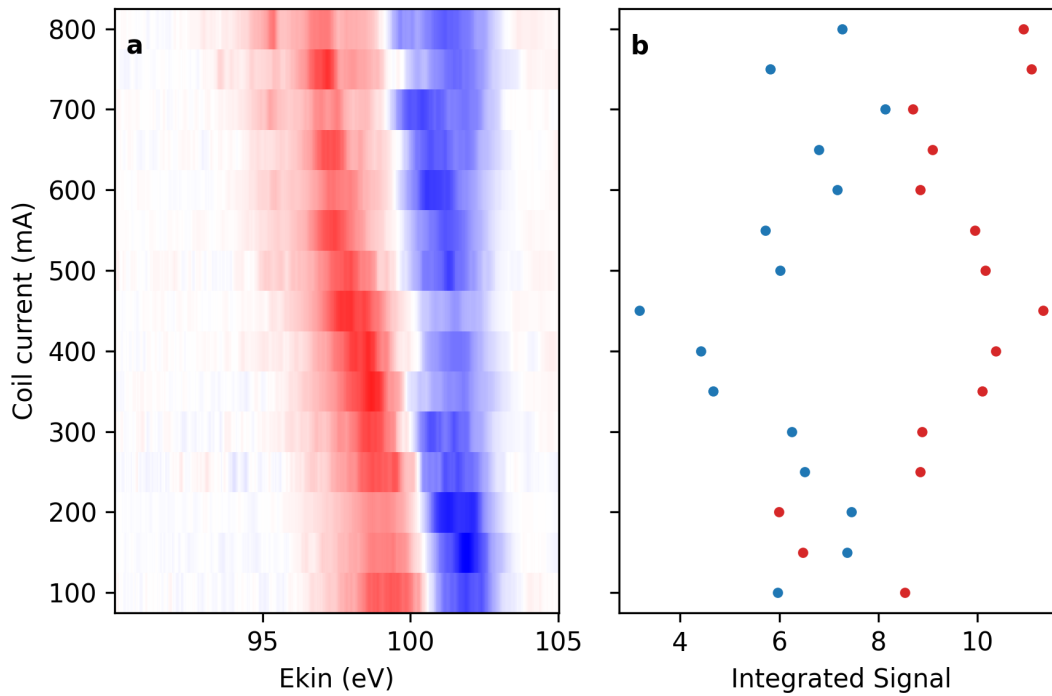


Figure S2: Scan of the coil current on the flight tube at 272 eV x-ray photon energy and -80 V retardation. a: false-color representation of the difference spectra of the photoline. b: integrated signal of positive (red) and negative (blue) contributions.

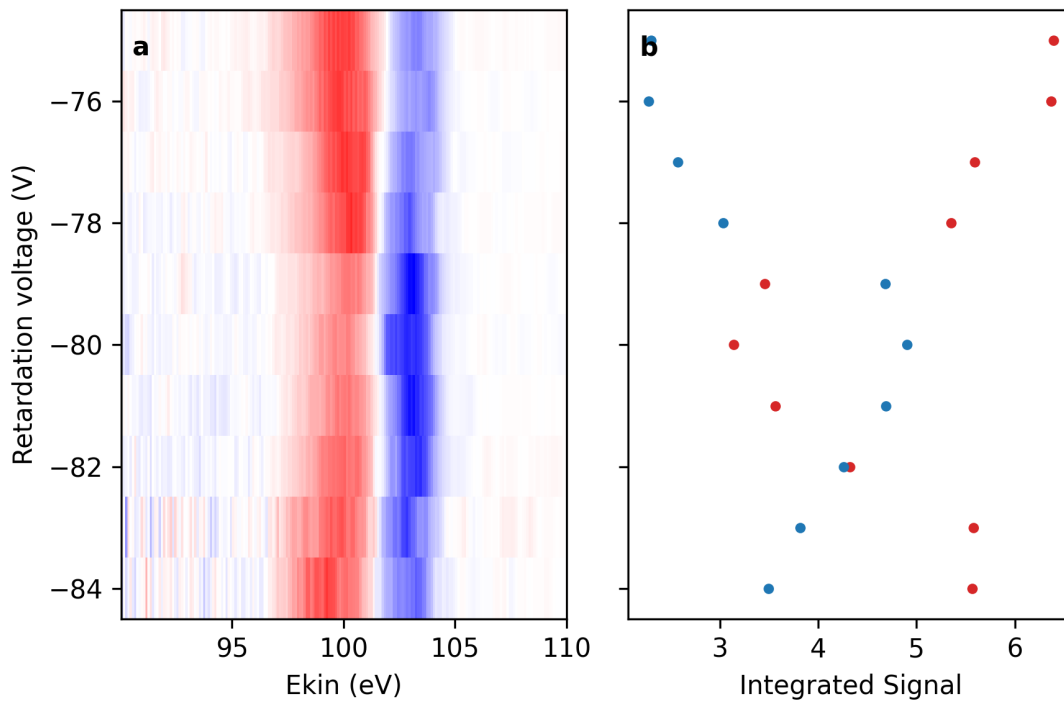


Figure S3: Scan of the retardation voltage at 272 eV and 200 mA coil current. a: false-color representation of the difference spectra of the photoline. b: integrated signal of positive (red) and negative (blue) contributions.

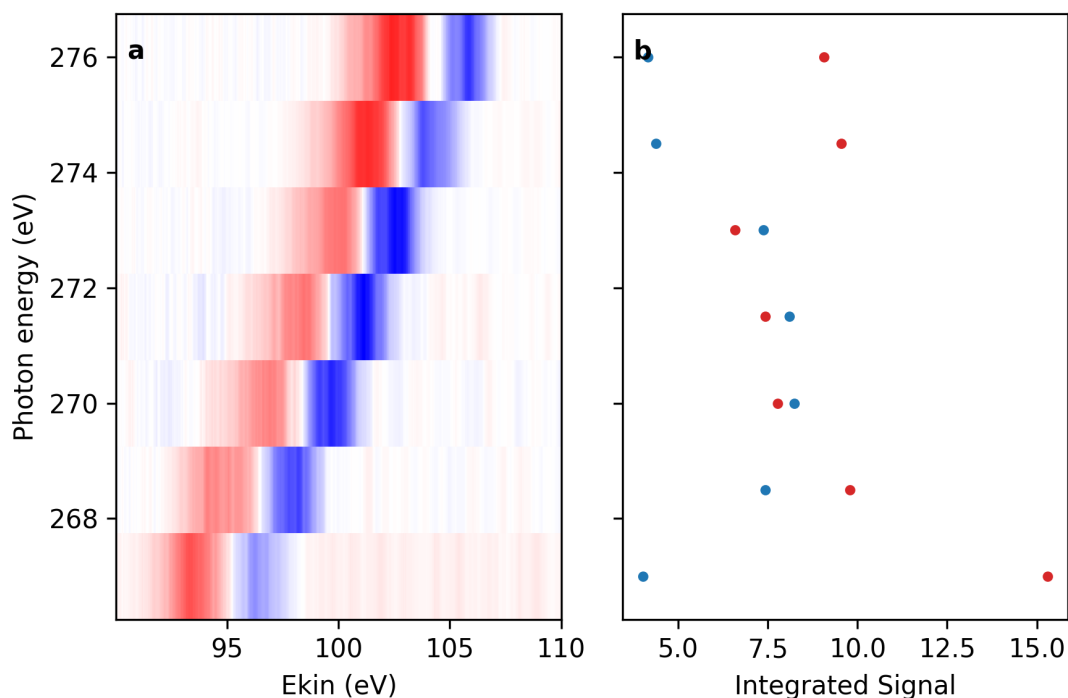


Figure S4: Scan of the photon energy at 80V retardation and 200mA coil current. a: false-color representation of the difference spectra of the photoline. b: integrated signal of positive (red) and negative (blue) contributions.

3 Quantum chemical results

The structure and the atom numbering of 2-thiouracil is shown in Fig. S5. The most relevant molecular orbitals involved in the valence excitations are depicted in Fig. S6 for the Franck-Condon geometry. The singlet states S_1 and S_2 have $n\pi^*$ and $\pi\pi^*$ character, respectively. At planar geometries, they originate from $27a' \rightarrow 7a''$ and $6a'' \rightarrow 7a''$ transitions. The triplet states T_1 and T_2 originate mainly from the same transitions of S_2 and S_1 , apart from the spin-flipping, and therefore they have $\pi\pi^*$ and $n\pi^*$ character, respectively. T_3 has a $\pi\pi^*$ character and is mostly contributed by the transitions $5a'' \rightarrow 7a''$ and, to a lesser extent, $6a'' \rightarrow 8a''$.

Table S2 reports the main structural parameters of the optimized geometries. The planar equilibrium structures are indicated by an asterisk ($S_{0,\min}^*$, $S_{1,\min}^*$, etc.); the non-planar geometry optimization of the states T_2 and T_3 did not converge to a stationary point. At all minima, except for $T_{1,\min}^*$, the C–S bond is elongated by ≈ 0.1 Å as compared to $S_{0,\min}$. A larger elongation of about 0.25 Å is found in the state S_2 . In the ground state the difference between the planar and non-planar minima $S_{0,\min}^*$ and $S_{0,\min}$ is negligible. In contrast, the states S_1 , S_2 and T_1 have non-planar minima which are depicted in Fig. S6 and involve an out-of-plane distortion of the C–S bond, with pyramidalization angles in the range $\approx 35^\circ$ – 50° . The stabilization energy,

associated with this out-plane distortion, is 0.30 eV, 0.48 eV and 0.17 eV for S_1 , S_2 and T_1 , respectively.

The comparison between Table S2 and Table 2 of Ref. ⁴ shows that the present optimized gas phase geometries agree very well with those obtained using the multi-state CASPT2 method. The main notable difference is a somewhat higher value of the pyramidalization angle ρ_{10324} , around the N atom bridging the C=S and C=O groups. Table S3 reports instead the non-planar and nearly planar minima obtained in Ref. ⁵ for 2-thiouracil in the presence of water solvent charges, which also agree nicely with the structures found in this work. This suggests that the same sets of geometries can be in principle visited by the wave packet both in the gas phase and in solution.

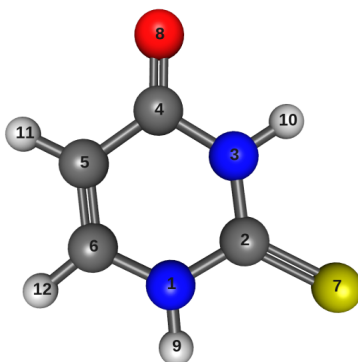


Figure S5: Structure and atom numbering of 2-thiouracil. The carbons are gray, the nitrogens are blue, the hydrogens are white, the oxygen is red and the sulphur is yellow.

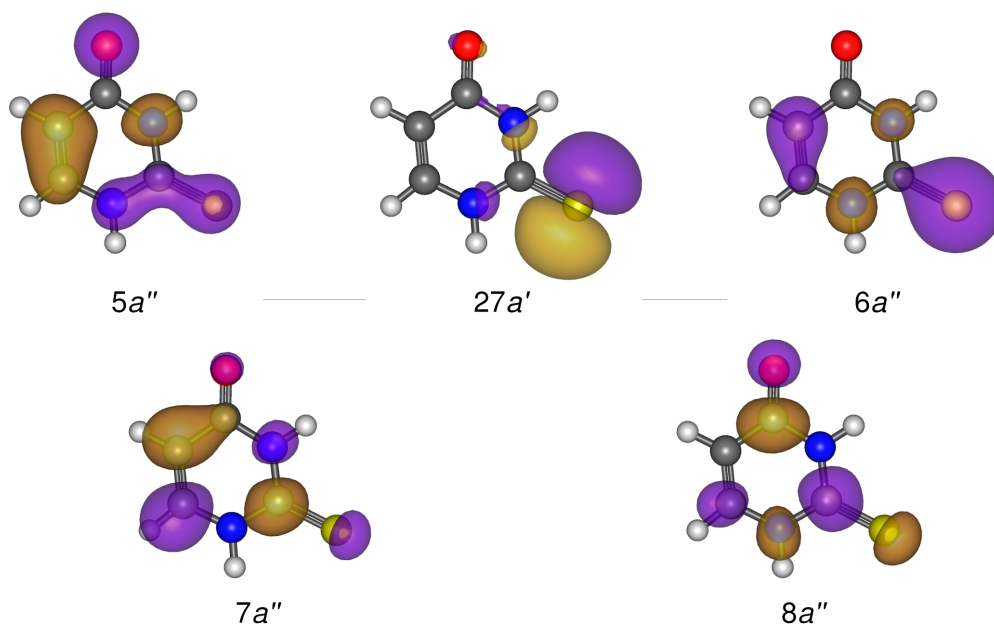


Figure S6: Most relevant orbitals involved in the valence excitations of 2-thiouracil, evaluated at the $S_{0,\min}^*$ geometry.

r_{34}	1.41	1.40	1.41	1.40
r_{45}	1.47	1.47	1.47	1.47
r_{56}	1.35	1.35	1.35	1.36
r_{61}	1.38	1.38	1.38	1.37
r_{27}	1.65	1.77	1.90	1.77
r_{48}	1.21	1.21	1.21	1.21
α_{127}	122.8	116.8	110.6	113.6
α_{348}	120.4	121.0	120.9	121.2
ρ_{7213}	-1.5	34.0	48.8	42.5
ρ_{8435}	-0.6	-3.2	0.8	2.1
ρ_{10324}	8.0	19.8	-10.8	-22.1
ρ_{12651}	1.5	-2.5	0.5	0.7

Table S2: Geometrical parameters of the planar and non-planar equilibrium structures of the lowest electronic states of 2-thiouracil, optimized at the (EOM-)CCSD/6-311++G** level. The largest structural changes with respect to $S_{0,\min}$ are highlighted in boldface. The bond distances r_{ij} are given in Å, the valence angles α_{ijk} and the pyramidalization angles ρ_{ijkl} are in degrees. ρ_{ijkl} is defined as the angle between the vector of the $i-j$ bond and the $ijkl$ plane. The dimension for the bond lengths is Å, for angles it is degrees.

	(nearly) planar geometries				
	$S_{0,\min}^*$	${}^1n\pi^*_{\min}$	${}^1\pi\pi^*_{\min}$	${}^3\pi\pi^*_{\min}$	${}^3n\pi^*_{\min}$
r_{12}	1.36	1.34	1.33	1.35	1.32
r_{23}	1.37	1.37	1.34	1.39	1.35
r_{34}	1.38	1.44	1.46	1.41	1.45
r_{45}	1.43	1.40	1.39	1.41	1.39
r_{56}	1.36	1.41	1.41	1.44	1.41

r_{61}	1.36	1.37	1.41	1.35	1.40
r_{27}	1.65	1.74	1.73	1.69	1.74
r_{48}	1.25	1.25	1.27	1.25	1.25
α_{127}	123.9	122.3	120.8	123.1	121.2
α_{348}	120.5	116.2	115.9	117.2	115.9
ρ_{7213}	0.0	-1.2	-0.2	0.1	-1.6
ρ_{8435}	0.3	1.2	-0.2	1.3	1.1
ρ_{10324}	-9.0	-19.1	-11.2	-10.7	-11.2
ρ_{12651}	-0.3	-6.6	-7.8	-4.1	-3.5
non-planar geometries					
	$S_{0,\min}$	${}^1n\pi^{*'}_{\min}$	${}^1\pi\pi^{*'}_{\min}$	${}^3\pi\pi^{*'}_{\min}$	${}^3n\pi^{*'}_{\min}$
r_{12}	1.36	1.39	1.37	1.39	1.39
r_{23}	1.37	1.41	1.39	1.41	1.41
r_{34}	1.38	1.38	1.38	1.37	1.37
r_{45}	1.43	1.44	1.44	1.44	1.45
r_{56}	1.36	1.37	1.37	1.38	1.37
r_{61}	1.36	1.35	1.36	1.34	1.36
r_{27}	1.65	1.79	1.86	1.77	1.78
r_{48}	1.25	1.25	1.24	1.25	1.25
α_{127}	123.9	118.4	112.6	115.8	111.2
α_{348}	120.5	119.7	120.9	120.6	120.9
ρ_{7213}	-0.0	32.2	45.6	37.5	41.5
ρ_{8435}	0.3	-1.5	0.3	0.4	0.0
ρ_{10324}	-9.0	9.5	4.2	6.7	6.5
ρ_{12651}	-0.3	-0.1	0.6	0.2	-0.4

Table S3: Geometrical parameters of the nearly planar and non-planar equilibrium structures of the lowest electronic states of 2-thiouracil, reported by Teles-Ferreira et al.⁵. The largest structural changes with respect to $S_{0,\min}$ are highlighted in boldface. The bond distances r_{ij} are given in Å, the valence angles α_{ijk} and the pyramidalization angles ρ_{ijkl} are in degrees. ρ_{ijkl} is defined as the angle between the vector of the $i-j$ bond and the $ijkl$ plane. The dimension for the bond lengths is Å, for angles it is degrees.

The EOM-CCSD electronic energies at the planar and non-planar minima of the different electronic states are reported in Table S4 and plotted in Fig. S8. The excitation energies at the ground state equilibrium ($S_{0,\min}$) are larger by ≈ 0.4 eV compared to those obtained by multi-reference calculations, although the spacing between the levels is similar. Indeed, the $S_2 \leftarrow S_0$ vertical excitation energy agrees quite well with the experimental gas phase UV absorption spectrum of thiouracil⁶. As shown in Fig. S8, the potential energy surfaces of the states S_1 and T_2 , both of $n\pi^*$ character are nearly parallel.

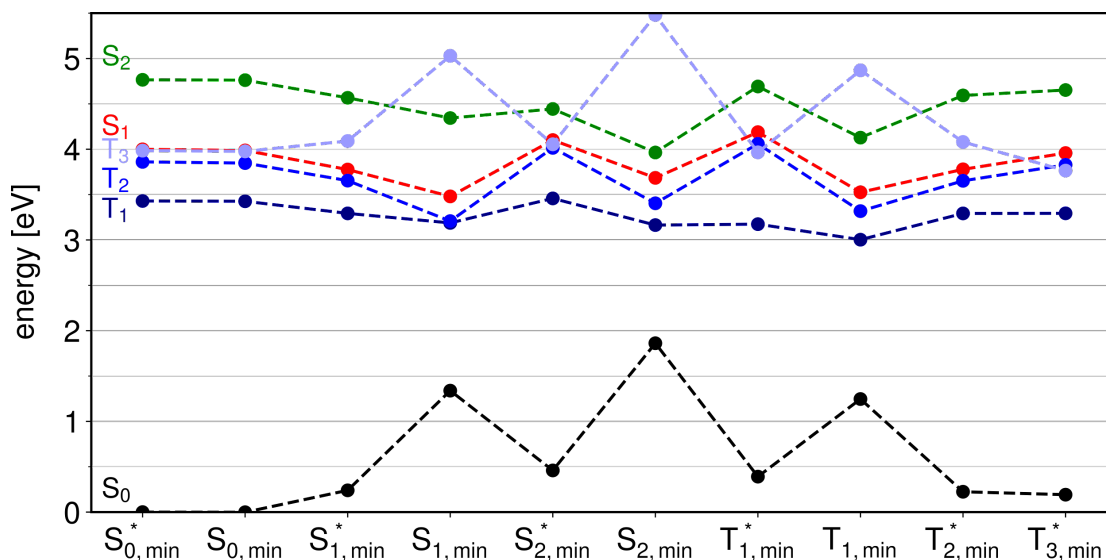


Figure S8: EOM-CCSD/6-311++G** electronic energies of the lowest singlet and triplet states of 2-thiouracil, calculated at the planar and non-planar minima of the different states.

	State	
--	-------	--

	S ₀	S ₁	S ₂	T ₁	T ₂	T ₃
	-	¹ (27a'→7a'')	¹ (6a''→7a'')	³ (6a''→7a'')	³ (27a'→7a'')	³ (5a''→7a'')
S* _{0,min}	0.00	4.00	4.77	3.43	3.86	3.98
S _{0,min}	0.00	3.99	4.76	3.43	3.85	3.98
S* _{1,min}	0.24	3.78	4.57	3.29	3.65	4.09
S _{1,min}	1.34	3.48	4.34	3.19	3.21	5.03
S* _{2,min}	0.46	4.10	4.44	3.46	4.02	4.05
S _{2,min}	1.86	3.68	3.96	3.16	3.40	5.48
T* _{1,min}	0.39	4.19	4.69	3.17	4.06	3.97
T _{1,min}	1.25	3.53	4.13	3.00	3.32	4.87
T* _{2,min}	0.22	3.78	4.59	3.29	3.65	4.08
T* _{3,min}	0.19	3.96	4.65	3.29	3.82	3.76

Table S4. EOM-CCSD/6-311++G** electronic energies (in eV) of the lowest singlet and triplet states of 2-thiouracil, calculated at the planar and non-planar minima of the different states. For each state the dominant orbital transitions are reported. Energies are given in eV.

4 Calculated state- and geometry-dependent pump-probe XPS spectra

Photoelectron spectra are calculated at different geometries considering an ionisation process starting from the states S₁, S₂, T₁, T₂ and T₃. The reference “pump-off” spectrum, with ionisation starting from S₀, is calculated only at the ground state minimum. For each geometry x the spectrum $\sigma_n^x(E)$ from the state n is given as a sum of contributions associated with the three 2p orbitals,

$$\sigma_n^x(E) = C \sum_{i=1}^3 A_{in}^x g(E - E_{in}^x),$$

where C is a constant, E_{in}^x is the ionization potential from the 2p_i orbital for the state n at the geometry x, evaluated by the EOM-IP-CCSD approach, and A_{in}^x is the ionization probability, approximated as the geometric average between the norms of the left and right Dyson orbitals⁷. The function g(·) is used to broaden the stick transitions in order to allow the comparison with

experiment; the calculated profiles are obtained by applying a Gaussian broadening with a standard deviation of 1.5 eV. Since in the EOM-IP-CCSD procedure the valence excited states are described by unrestricted wavefunctions, the two binding energies for the α and β electrons differ by 0.0-0.1 eV and have been averaged in the calculation of E_{in}^x .

The (geometry-dependent) pump-probe signal $S_n^x(E)$, associated with population on a given state, is obtained as the difference

$$S_n^x(E) = \sigma_n^x(E) - \sigma_{S_0}^{S_{0,min}}(E).$$

The calculated pump-probe spectra are shown in Figures S9 and S10 for the planar and non-planar geometries, respectively. Note the general trend for the binding energies $T_3 < S_2 < T_1 < S_1 \approx T_2$.

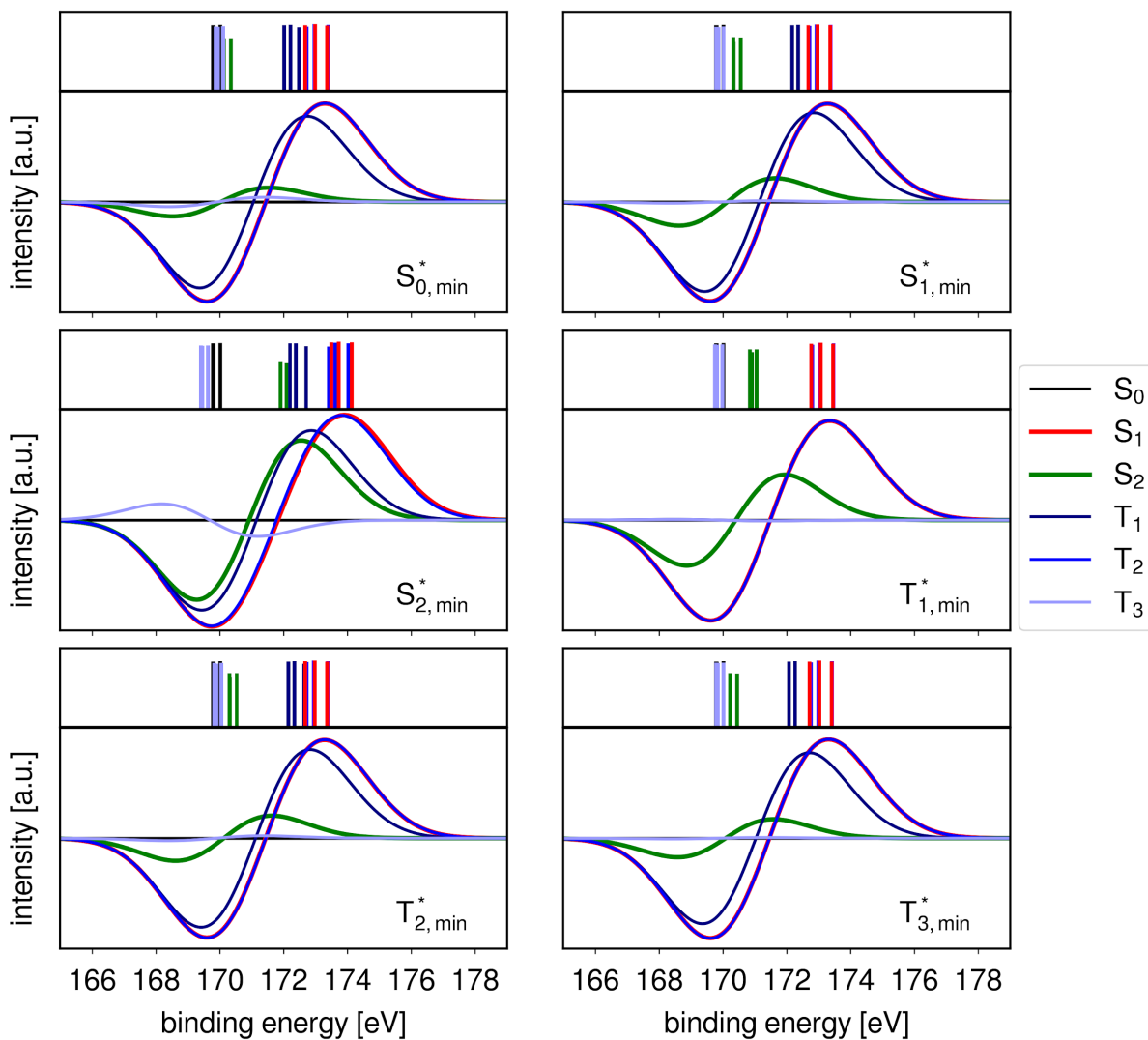


Figure S9: Binding energies of the 2p electrons (top panels) and pump-probe spectra (bottom panels) evaluated for different electronic states and different planar stationary geometries. The ionization intensities are estimated using Dyson orbital norms.

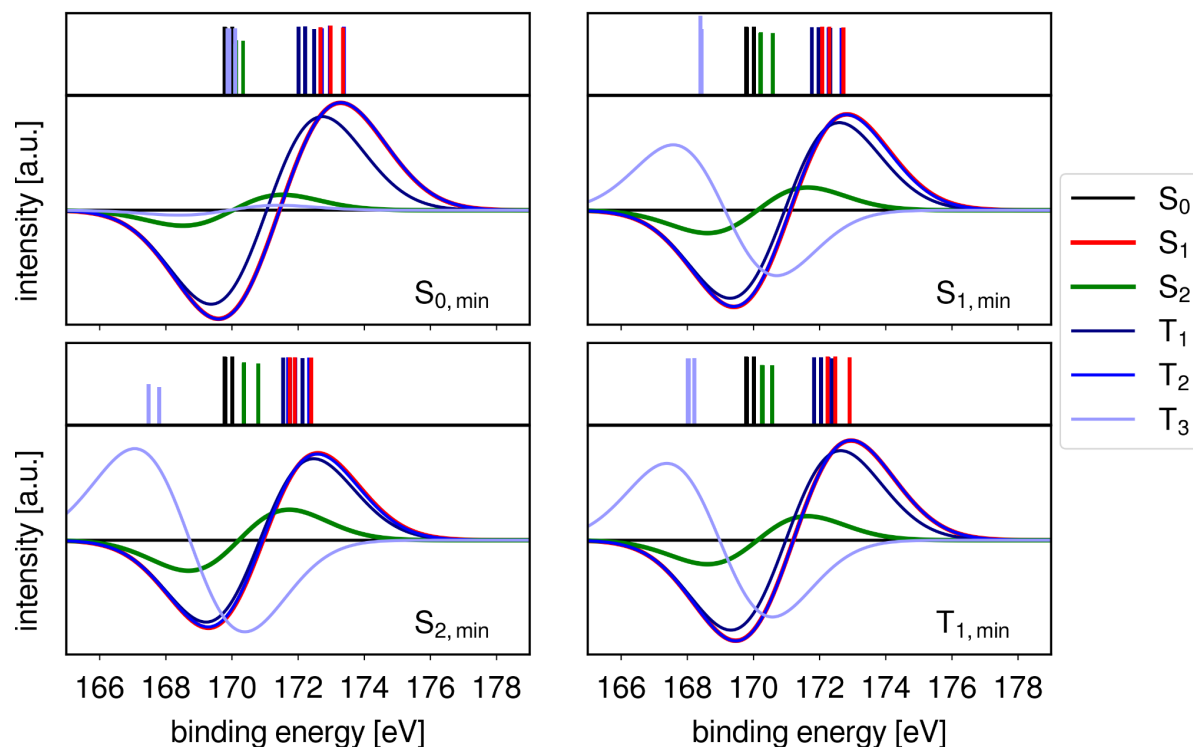


Figure S10: Binding energies of the 2p electrons (top panels) and pump-probe spectra (bottom panels) evaluated for different electronic states and different fully optimized geometries. The ionization intensities are estimated using Dyson orbital norms.

Soft X-ray photoelectron probing of the excited-state dynamics of 2-thiouracil. (a) Calculated electronic energies for the valence excited states, in the range 0-6 eV, and the core ionised states, in the range 170-179 eV, for four geometries relevant in the short time dynamics. The arrows illustrate the 2p-1 ionisation process associated with the most intense transition. The core ionised states are grouped into sets of three states, which follow the color coding of the valence states, meaning that their valence configuration is maintained with a p_x , p_y or p_z core hole. Accordingly, the electron kinetic energy E_{kin} refers to ionisations out of S_0 , S_1 and S_2 , depending on the geometry. (b). Partial charges on the S atom plotted against the binding energy of the 2p electrons, calculated for the valence states at nine different geometries. For each geometry, the graph includes three dots for each excited state (S_1 , S_2 , T_1 , T_2 , T_3); in addition, three dots are included for the ionisation from S_0 at S_0^*,min , for a total of $9 \times 3 \times 5 + 3 = 138$ dots.

5 Potential model fits

We extend the discussion of Figure 4b of the main text. Although the linear trend is already visible in Figure 4b, the relation between the local charge and binding energy (or excited state

chemical shift) becomes even more obvious, when taking geometrical effects into account. In this, we closely follow the potential model as introduced by Gelius ⁸.

We fit two different versions of the potential model. Model A is a simple linear relation between the binding energy E_{bind} and local charge at the probed atom (sulphur) Q_S :

$$E_{\text{bind}} = k * Q_S + l,$$

with k and l as fit constants.

We use the calculated Löwdin charges to perform a fit and deduce k and l from the dataset in Figure 4b. The values from this fit are plotted against the model potential binding energy on the x-axis and the ab initio binding energy on the y-axis in Figure S11. This model leads to an R^2 of 0.82.

A better fit can be obtained when taking the charge and geometry of the environment of the sulphur atom into account:

$$E_{\text{bind}} = k * Q_S + \sum_{A \neq S} Q_A / R_{AS} + l,$$

where the Q_A are the charges at all other atoms at their respective distances to the probed sulphur atom R_{AS} . The result of the fit is shown in Figure S12. It makes the fit even better increasing the R^2 from 0.82 in the simple linear potential model to 0.92 in the more sophisticated potential model.

The remaining discrepancies between the potential model and the ab initio binding energies are due to final state effects including electronic relaxation. These effects have been discussed in the static literature (see for example Ref. ⁹).

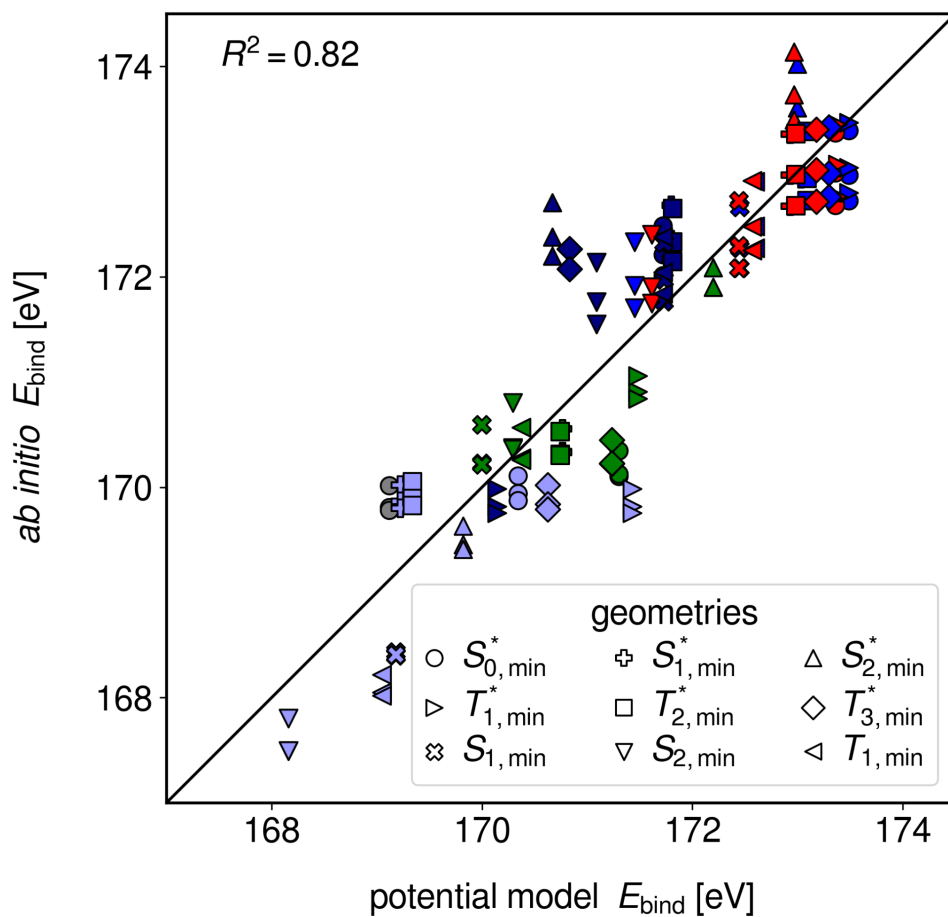


Figure S11: Binding energy from the ab initio calculations vs binding energy from the simple potential model for the dataset in Figure 4b.

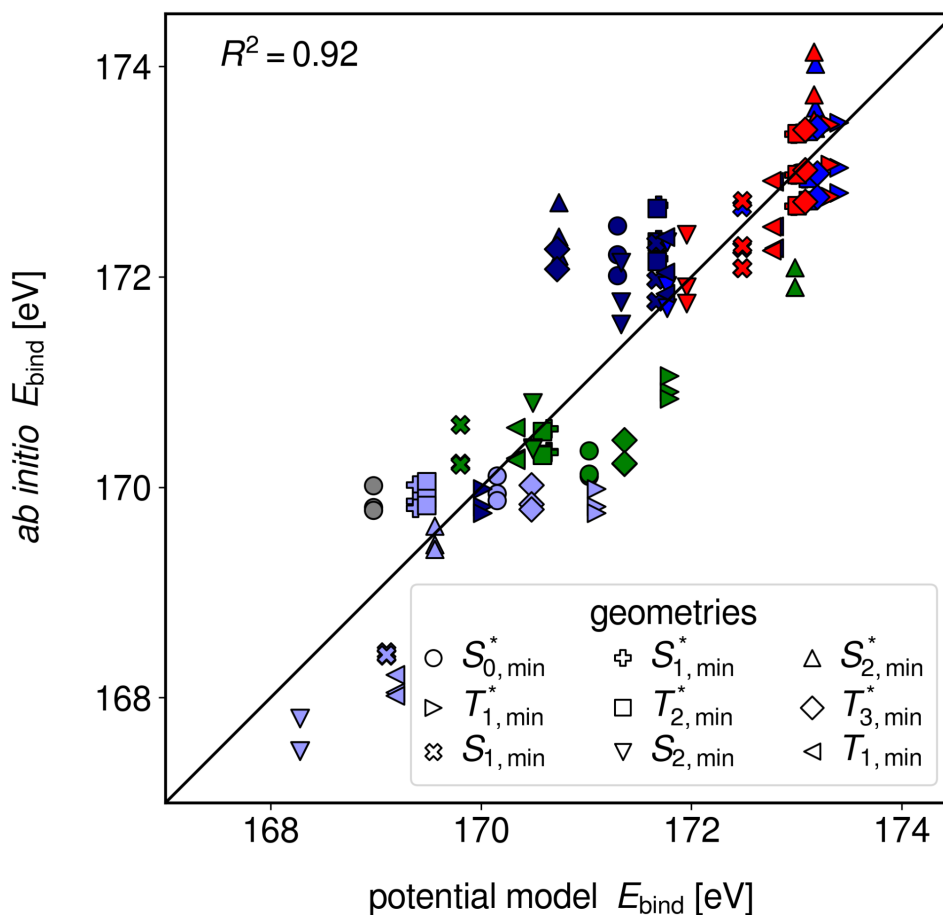


Figure S12: Same as Figure S10 but using a geometrically corrected potential model.

6 Exceptions in the clustering according to electronic state

The data of Table S2 allow us to explain the exceptions in the clustering according to electronic states reported in Figure 4(b) of the main text. For example, the dots for the T_1 state at the planar T_1 minimum ($T_{1,\min}^*$) are quite separated from the rest of the T_1 cluster. A probable reason is that this geometry is quite similar to the Frank-Condon (FC) point, except for a slight elongation of the C=C bond. In particular, in contrast to the other excited state minima, the C-S bond distance is relatively short. Therefore, it is easier for the electron hole created by UV excitation on the S atom to redistribute partially on the neighbouring atoms. Then, the 2p binding energy decreases.

The opposite is true for the dots of the S_2 state at the planar S_2 minimum ($S_{2,\min}^*$). Indeed, among the planar geometries, this is the one with the largest C-S bond distance, so that the hole is more likely to localize on the S atom.

Note that, although these points shift away from their clusters, the shift always correlates with the electron binding energy: the higher the partial charge on the S atom, the higher the ionization potential.

7 Pulse energy scans

Power-dependent scans were performed for x-ray only probing (Fig. S13) to assure that the x-ray induced photoelectron signal is not saturated. The resulting x-ray pulse energy distribution used in the experiment is shown in Fig. 13c. Similarly, UV-power scans were performed (Fig. S13) to avoid UV induced saturation effects. Here, the absolute of the total difference intensity is plotted as a function of UV pulse energy. The resulting pulse energy histogram with energies in the linear excitation regime is given in Fig. S13d.

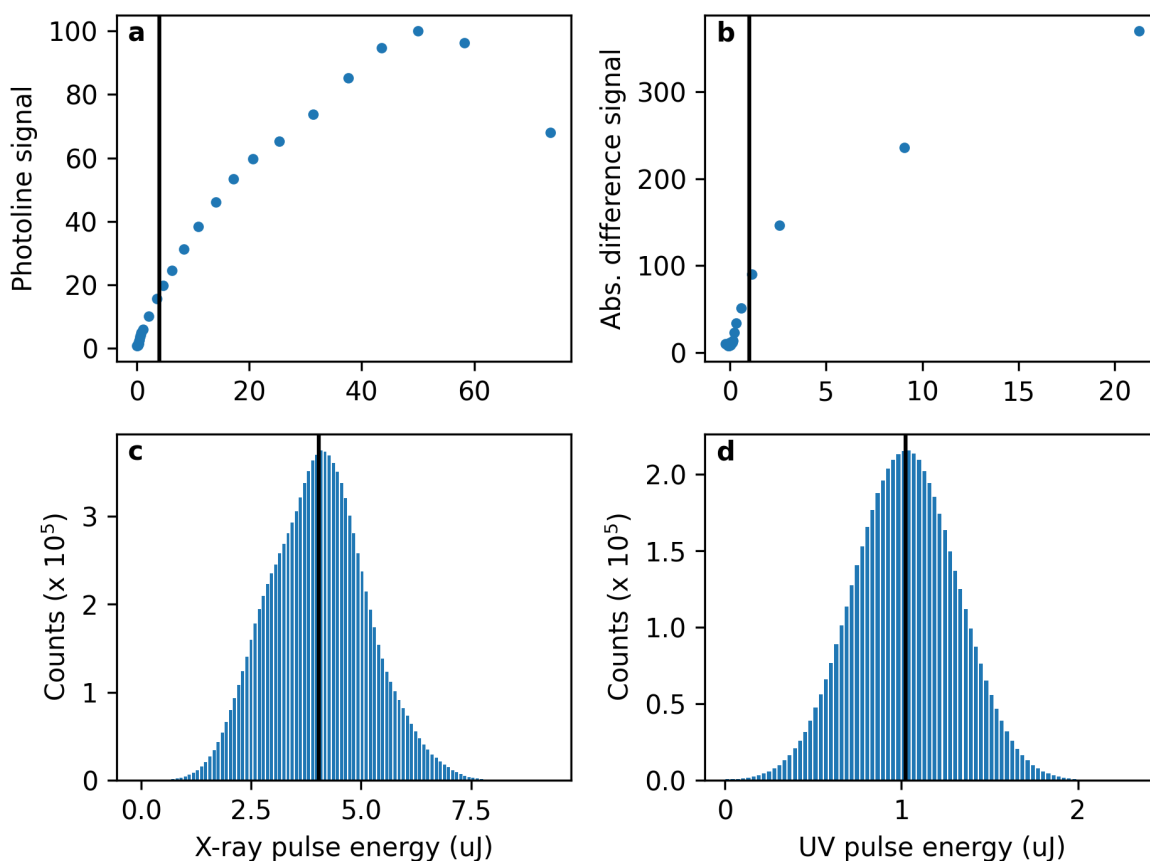


Figure S13: a: X-ray-only S2p photoelectron signal as a function of x-ray pulse energy. b: Integrated absolute difference signal at S2p photoline as a function of UV pulse energy. c and d: X-ray and UV pulse energy distribution for the experimental data shown in the paper. The vertical black lines mark the centre of gravity of the distributions. They are also inserted in a & b for comparison to the pulse energy scans.

8 Data handling

The data presented covers about 8 million FEL shots. All electron time-of-flight traces have been normalised on FEL pulse energy prior to further processing. As shot-to-shot FEL photon energies are not delivered by FLASH, long term drifts and trends over the FEL pulse train have been tracked with the sulphur 2p photoline itself and corrected via self-referencing the photoline using the following procedure.

In order to determine the photoline position in the time-of-flight spectra better, a number of 200 consecutive pulse trains (20s of data, 50 pulses per train) were averaged pulse-wise. The resulting 50 spectra were fitted with a Gaussian function within a 200 ns window around the expected photoline position. However, only every second shot can be used to evaluate the influence of the FEL on the spectrum as the other half was additionally influenced by the UV pump. The trend over pulse train of the remaining 25 values is fitted with a second order polynomial. The resulting curve is used to shift the original 10,000 raw spectra. To track not only the trends over the pulse trains but also long term shifts, the overall mean of the photoline position of the first of those processed data chunks is set as a global reference. The raw spectra for all data chunks are shifted towards this reference utilizing the (for each chunk determined) pulse train trend of the average spectra.

After that, shot-to-shot difference spectra were calculated and the resulting spectra were binned by delay. The delays were corrected by means of the bunch arrival monitor (BAM) which measures the arrival of the electron bunches and thus gives information on the arrival time jitter of the x-ray pulses^{1,2}. The delay binning was chosen in such a way that all bins have similar statistics (~73,000 shot pairs per bin). In combination with the delay correction via BAM, this allows a finer binning for delays close to time-zero than experimentally set.

References

1. Schulz, S. *et al.* Femtosecond all-optical synchronization of an X-ray free-electron laser. *Nat Commun* **6**, 5938 (2015).
2. Savelyev, E. *et al.* Jitter-correction for IR/UV-XUV pump-probe experiments at the FLASH free-electron laser. *New J. Phys.* **19**, 043009 (2017).
3. Kruit, P. & Read, F. H. Magnetic field paralleliser for 2π electron-spectrometer and electron-image magnifier. *J. Phys. E: Sci. Instrum.* **16**, 313–324 (1983).
4. Mai, S., Marquetand, P. & González, L. A Static Picture of the Relaxation and Intersystem Crossing Mechanisms of Photoexcited 2-Thiouracil. *J. Phys. Chem. A* **119**, 9524–9533 (2015).
5. Teles-Ferreira, D. C. *et al.* A Unified Experimental/Theoretical Description of the Ultrafast Photophysics of Single and Double Thionated Uracils. *Chem. Eur. J.* **26**, 336–343 (2020).
6. Khvorostov, A., Lapinski, L., Rostkowska, H. & Nowak, M. J. UV-Induced Generation of Rare Tautomers of 2-Thiouracils: A Matrix Isolation Study. *J. Phys. Chem. A* **109**, 7700–7707 (2005).
7. Vidal, M. L., Krylov, A. I. & Coriani, S. Dyson orbitals within the fc-CVS-EOM-CCSD framework: theory and application to X-ray photoelectron spectroscopy of ground and excited states. *Phys. Chem. Chem. Phys.* **22**, 2693–2703 (2020).
8. Gelius, U. Binding Energies and Chemical Shifts in ESCA. *Phys. Scr.* **9**, 133–147 (1974).
9. Mårtensson, N. & Nilsson, A. On the origin of core-level binding energy shifts. *J. Electr. Spectr. Rel. Phen.* **75**, 209–223 (1995).